J. Fluid Mech. (1997), *vol.* 351, *pp.* 41–74. Printed in the United Kingdom

On the instantaneous cutting of a columnar vortex with non-zero axial flow

By J. S. MARSHALL AND S. KRISHNAMOORTHY

Department of Mechanical Engineering and Iowa Institute of Hydraulic Research,
The University of Iowa, Iowa City, IA 52242, USA

(Received 9 October 1996 and in revised form 8 April 1997)

A study of the response of a columnar vortex with non-zero axial flow to impulsive cutting has been performed. The flow evolution is computed based on the vorticity–velocity formulation of the axisymmetric Euler equation using a Lagrangian vorticity collocation method. The vortex response is compared to analytical predictions obtained using the plug-flow model of Lundgren & Ashurst (1989). The plug-flow model indicates that axial motion on a vortex core with variable core area behaves in a manner analogous to one-dimensional gas dynamics in a tube, with the vortex core area playing a role analogous to the gas density. The solution for impulsive cutting of a vortex obtained from the plug-flow model thus resembles the classic problem of impulsive motion of a piston in a tube, with formation of an upstream-propagating vortex 'shock' (over which the core radius changes discontinuously) and a downstream-propagating vortex 'expansion wave' on opposite sides of the cutting surface. Direct computations of the vortex response from the Euler equation reveal similar upstream- and downstream-propagating waves following impulsive cutting for cases where the initial vortex flow is subcritical. These waves in core radius are produced by a series of vortex rings, embedded within the columnar vortex core, having azimuthal vorticity of alternating sign. The effect of the compression and expansion waves is to bring the axial and radial velocity components to nearly zero behind the propagating vortex rings, in a region on both sides of the cutting surface with ever-increasing length. The change in vortex core radius and the variation in pressure along the cutting surface agree very well with the predictions of the plug-flow model for subcritical flow after the compression and expansion waves have propagated sufficiently far away. For the case where the ambient vortex flow is supercritical, no upstream-propagating wave is possible on the compression side of the vortex, and the vortex axial flow is observed to impact on the cutting surface in a manner similar to that commonly observed for a non-rotating jet impacting on a wall. The flow appears to approach a steady state near the point of impact after a sufficiently long time. The vortex response on the expansion side of the cutting surface exhibits a downstream-propagating vortex expansion wave for both the subcritical and supercritical conditions. The results of the vortex response study are used to formulate and verify predictions for the net normal force exerted by the vortex on the cutting surface. An experimental study of the cutting of a vortex by a thin blade has also been performed in order to verify and assess the limitations of the instantaneous vortex cutting model for application to actual vortex–body interaction problems.

1. Introduction

Vortex impact with thin blades or bodies occurs in several common rotorcraft operations, including ingestion of atmospheric turbulence by the main rotor and impact of vortices generated by the main rotor on the tail section of the vehicle. Such interactions can generate impulsive forces and moments on the helicopter, resulting in degradation of vehicle control and undesirable noise production (Sheridan & Smith 1978; Leverton, Pollard & Wills 1977). The unsteady forces and noise production caused by vortex impact of this sort have been studied by a number of investigators, both from an experimental viewpoint (Ahmadi 1986; Cary 1987; Johnston & Sullivan 1992; Liou, Komerath & McMahon 1990; Bagai & Leishman 1992; Affes *et al.* 1993) and using idealized theoretical models (Affes & Conlisk 1993; Affes, Xiao & Conlisk 1994; Amiet, Simonich & Schlinker 1990; Howe 1988, 1989; Simonich *et al.* 1990; Marshall & Yalamanchili 1994). Recent reviews of work in this area are given by Kim & Komerath (1995) and Doligalski, Smith & Walker (1994).

The vortex–body impact problem is complicated by the fact that several regimes of interaction exist, which are not always clearly distinguished in the existing literature, and models of the flow which may be appropriate to one regime typically are not applicable to another regime. The regimes of interaction are determined both by the *impact parameter* $2\pi\sigma U/\Gamma$, which is the ratio of the relative impact velocity U of the vortex on the body to the maximum vortex swirl velocity $\Gamma/2\pi\sigma$, and by the *thickness parameter* T/σ, which is the ratio of some measure of body 'thickness' T to the vortex core radius σ. For low and moderate values of $2\pi\sigma U/\Gamma$, the swirling motion of the vortex causes the boundary layer on the body surface to separate from the body and wrap about the vortex before impact of the vortex core on the body. As $2\pi\sigma U/\Gamma$ is increased, the vorticity ejection from the body surface occurs when the body is at a progressively closer distance to the vortex, such that less wrapping of the secondary vorticity occurs prior to impact of the primary vortex on the body.

For values of $2\pi\sigma U/\Gamma$ which are sufficiently high, the nature of the vortex–body interaction depends on the value of the parameter T/σ. For large values of T/σ, the vortex is stretched about the body surface (Affes & Conlisk 1993; Marshall & Yalamanchili 1994), such that eventually the vortex core becomes sufficiently small and the body surface comes sufficiently close to the vortex that separation of the body boundary layer will occur. After separation, the ejected boundary layer vorticity will again wrap about the vortex core, leading to disruption of the primary vortex. It is this regime, for instance, to which most of the physical processes discussed in the review by Kim & Komerath (1995) apply.

The third regime occurs for small values of T/σ and high values of $2\pi\sigma U/\Gamma$, for which case there is no boundary layer separation and very little vortex deformation prior to vortex impact on the body (Marshall & Yalamanchili 1994). Typical interaction events in this regime might include chopping of a vortex by a thin blade. The penetration of the blade into the vortex core gives rise to a 'penetration force' which is directed parallel to the direction of blade motion relative to the vortex centroid. A number of investigators have constructed theoretical models of unsteady force and noise generation from vortex chopping; however, these models typically make strong assumptions regarding the vortex response to cutting. For instance, for the case of a vortex with no axial flow, Howe (1989) and Simonich *et al.* (1990) assume that the vortex evolves according to rapid distortion theory (RDT) as it comes close to the body, and Howe (1989) also utilizes the thin-airfoil approximation. The use of RDT for the penetration of a blade into the core of a vortex with no axial flow was recently

examined by Marshall & Grant (1996) by comparison of RDT results with direct simulation of the vortex response for different values of $2\pi\sigma U/\Gamma$.

For the case of chopping of a vortex with non-zero ambient axial flow, some of the acoustic studies (e.g. Howe 1988) assume that the vortex is 'frozen', so that the core radius does not change in time above or below the blade. In order to assess the range of validity of this frozen vortex approximation for computation of blade surface forces, it is necessary to clearly understand the nature of the vortex response to cutting and the associated time scales of the vortex response.

Marshall (1994) examined the response of a vortex with non-zero axial flow following instantaneous cutting using the plug-flow model of Lundgren & Ashurst (1989) for the vortex response. The plug-flow model is found to predict a 'vortex shock' (i.e. a discontinuity in vortex core radius) propagating upstream on the side of the vortex that is compressed by the axial flow and a vortex expansion wave (over which the core radius varies linearly between two constant values) propagating downstream on the opposite side of the vortex. The vortex shock increases the core radius near the blade while the vortex expansion wave decreases the core radius near the blade. The resulting difference in core radius on the two sides of the blade leads to a constant normal force on the blade directed normal to the blade surface. Krishnamoorthy & Marshall (1994) examined experimentally the far-field response of a vortex to sudden chopping by a thin flat plate and report observing a travelling vortex breakdown propagating upstream on the vortex following cutting, with about the same propagation speed as predicted by Marshall (1994) for the vortex 'shock'.

Lee *et al.* (1995) have recently performed direct numerical simulations (from the Euler equation) of the response of an axisymmetric vortex to impulsive cutting. Lee *et al.* report no upstream-propagating wave motion on the vortex core following cutting, but rather find that the vortex spreads out on the blade surface much like the flow that is observed when a non-swirling jet impinges on a flat surface. However, the results of Lee *et al.* are reported only for the compression side of the vortex and for a case where the ambient vortex flow is supercritical, such that the ambient axial velocity on the vortex core is larger than the phase velocity of axisymmetric waves (and no upstream-propagating waves are possible).

In this paper, we reconsider the numerical model proposed by Lee *et al.* (1995), in which an axisymmetric vortex with non-zero axial flow is instantaneously cut along a plane surface, and compare the results to the predictions of the plug-flow model. Different regimes of vortex response following cutting are observed depending on the value of the *axial flow parameter* $2\pi\sigma w_0/\Gamma$, which represents the ratio of the mean axial velocity within the core to the maximum vortex swirl velocity, including both upstream-propagating waves and jet-like behaviour on the compression side and expansion waves on the expansion side. The relationship of the vortex response to the pressure variation and the net force exerted on the cutting surface is examined. An experimental study of the near-field response of a vortex to cutting by a thin blade has also been performed, using fluorescent dye of two colours illuminated by a laser sheet to distinguish between vorticity within the centre vortex and that shed from the blade boundary layer. The experimental results are compared to the predictions of the plug-flow model and are used to determine the range of the parameter $2\pi\sigma U/\Gamma$ for which the instantaneous cutting model is valid.

The numerical computations are obtained from solution of the Euler equation in the vorticity–velocity formulation, using a vorticity collocation method for axisymmetric symmetric swirling flows recently presented by Marshall & Grant (1997). The computational method is briefly reviewed in §2. Results for the computed vortex

response for the expansion and compression sides of the cutting surface are described in §§3 and 4, respectively. Computational results for the pressure variation and net force on the cutting surface are given in §5 for subcritical flow and in §6 for supercritical flow. Experimental observations of the response of a columnar vortex following cutting by a thin blade are described in §7, and conclusions are given in §8.

2. Numerical method

The problem of the evolution of an axisymmetric inviscid vortex with non-zero axial flow following an instantaneous cut is simulated by numerical solution of the Euler equation in the vorticity–velocity formulation. The computation is initialized such that both the axial vorticity and the axial velocity distribution vary radially in proportion to $\exp(-r^2/\sigma_0^2)$, where σ_0 is referred to as the vortex core radius. At time $t = 0$, the vortex is 'cut' along the plane $z = 0$ by enforcing a condition of reflectional symmetry in the vorticity field over this plane. The flow both upstream and downstream of the cutting surface is simulated in separate calculations.

The flow evolution following cutting is simulated using the inviscid version of the Lagrangian vorticity collocation method of Marshall & Grant (1997) for axisymmetric swirling flows of an incompressible fluid. In this method, the vorticity is evolved on a set of N Lagrangian control points in the (r, z)-plane using transport equations for the components $(\omega_r, \omega_\theta, \omega_z)$ of vorticity of the form

$$\frac{\mathrm{d}\omega_r}{\mathrm{d}t} = \omega_r \frac{\partial u}{\partial r} + \omega_z \frac{\partial u}{\partial z}, \tag{1a}$$

$$\frac{\mathrm{d}\omega_\theta}{\mathrm{d}t} = \frac{\omega_\theta u}{r} - \frac{2\omega_r v}{r}, \tag{1b}$$

$$\frac{\mathrm{d}\omega_z}{\mathrm{d}t} = \omega_r \frac{\partial w}{\partial r} + \omega_z \frac{\partial w}{\partial z}, \tag{1c}$$

where $\mathrm{d}/\mathrm{d}t$ is the material derivative and (u, v, w) are the components of the velocity vector in the (r, θ, z) directions, respectively.

The radial boundary conditions on the vorticity components are $\omega_r = \omega_\theta = 0$ and $\partial\omega_z/\partial r = 0$ on the symmetry axis $r = 0$ and $\boldsymbol{\omega} \to 0$ faster than r^{-4} as $r \to \infty$. The far-field axial boundary condition on the vorticity is $\omega_z \to (\Gamma/\pi\sigma_0^2)\exp(-r^2/\sigma_0^2)$, $\omega_\theta \to (2Qr/\pi\sigma_0^4)\exp(-r^2/\sigma_0^2)$ and $\omega_r \to 0$ as $z \to \infty$, where Q is the axial flow rate. The reflectional boundary conditions about $z = 0$, which are used to enforce the no-penetration boundary condition for computations of the flow on either the expansion or compression sides, are given by $\omega_r(r, z, t) = \omega_r(r, -z, t)$, $\omega_\theta(r, z, t) = \omega_\theta(r, -z, t)$ and $\omega_z(r, z, t) = -\omega_z(r, -z, t)$. The flow is initialized with the same vorticity distributions as used for the $z \to \infty$ boundary conditions. A sketch showing the initial vortex flow and the cutting surface is given in figure 1.

The induced velocity is obtained by solution of the Biot–Savart integral, using an interpolation of the vorticity field based on a representation consisting of ring-like elements for points sufficiently far removed from the symmetry axis and blob-like elements for points lying on the symmetry axis. Ring-like elements are excluded from a region with radius R_E from the symmetry axis, which is usually taken to be of the order of the element radius. The vorticity representation may be expressed as

$$\boldsymbol{\omega}(\boldsymbol{x}, t) = \sum_{n=1}^{N} \boldsymbol{G}_n(t) f_n(\boldsymbol{x} - \boldsymbol{x}_n), \tag{2}$$

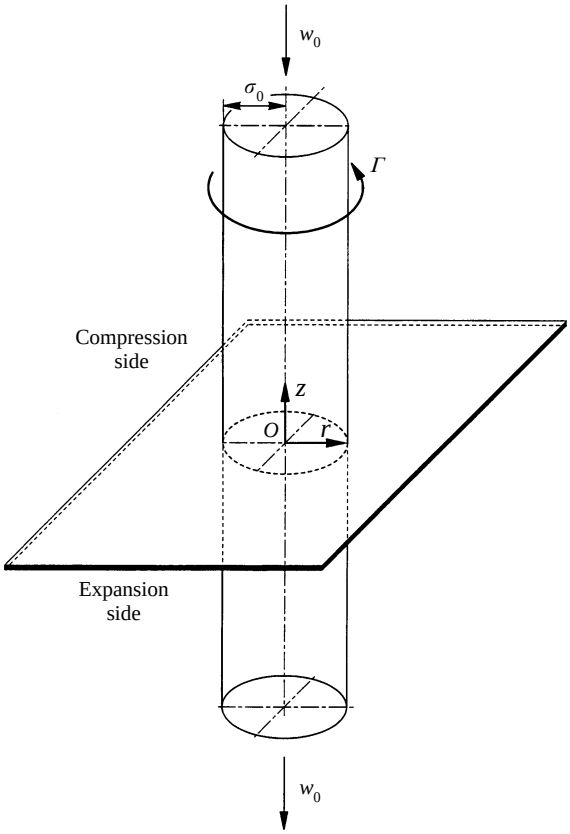

FIGURE 1. Sketch showing the initial vortex flow and the cutting surface. The vortex is divided into a *compression side* and an *expansion side*, on which the vortex is axially compressed or stretched by the ambient axial flow, respectively.

where the control point locations $\boldsymbol{x}_n(t)$ (i.e. the element centroids in the r, z-plane) are evolved as material points, according to

$$\frac{\mathrm{d}\boldsymbol{x}_n}{\mathrm{d}t} = \boldsymbol{u}(\boldsymbol{x}_n, t). \tag{3}$$

The element *amplitude* $\boldsymbol{G}_n$ represents the integral of vorticity associated with the control point over the element cross-section. The *weighting function* $f_n(\boldsymbol{x}-\boldsymbol{x}_n)$ specifies the distribution of vorticity within the element core and is normalized so that

$$\int_A f_n(\boldsymbol{x}-\boldsymbol{x}_n)\, r\, \mathrm{d}r\, \mathrm{d}z = r_n \tag{4a}$$

for the ring-like elements and as

$$\int_A f_n(\boldsymbol{x}-\boldsymbol{x}_n)\, r\, \mathrm{d}r\, \mathrm{d}z = R_E \tag{4b}$$

for the blob-like elements, where A denotes the entire (r, z)-plane and r_n is the radial position of control point n. In the present computations, both ring-like and blob-like elements are assumed to have Gaussian cross-section, so we write

$$f_n(\boldsymbol{x}-\boldsymbol{x}_n) = C_n \exp\left[-\frac{(z-z_n)^2+(r-r_n)^2}{\delta_n^2}\right], \tag{5}$$

where δ_n is the element radius. The normalization constant is obtained as

$$C_n = \frac{2r_n}{\pi^{1/2}\delta_n^3 + 2\pi r_n \delta_n^2} \tag{6a}$$

for ring-like elements and as

$$C_n = \frac{2R_E}{\pi^{1/2}\delta_n^3} \tag{6b}$$

for blob-like elements.

Substituting (2) into the Biot–Savart equation and integrating, using the method of Laplace integrals for small values of δ_n/r_n, the induced velocity from the nth ring-like element is obtained as

$$u_n(r,\theta,z,t) = \frac{(z-z_n)\,G_\theta k_n \xi_n}{4\pi(r_n r^3)^{1/2} k_n'^2}[(1-\tfrac{1}{2}k_n^2)\,E(k_n) - k_n'^2 K(k_n)], \tag{7a}$$

$$v_n(r,\theta,z,t) = -\frac{(z-z_n)\,G_r k_n \xi_n}{4\pi(r_n r^3)^{1/2} k_n'^2}[(1-\tfrac{1}{2}k_n^2)\,E(k_n) - k_n'^2 K(k_n)] - \frac{r_n G_z k_n \xi_n}{4\pi(r_n r^3)^{1/2} k_n'^2}\left[-k_n'^2 K(k_n) + \left\{1-\tfrac{1}{2}k_n^2\left(1+\frac{r}{r_n}\right)\right\}E(k_n)\right], \tag{7b}$$

$$w_n(r,\theta,z,t) = \frac{k_n G_\theta \xi_n}{8\pi(r_n r^3)^{1/2} k_n'^2}[(r+r_n)\,k_n^2 E(k_n) - 2r\{E(k_n) - k_n'^2 K(k_n)\}], \tag{7c}$$

where (G_r, G_θ, G_z) are the components of $\boldsymbol{G}_n$, k_n and k_n' are defined by

$$k_n^2 \equiv \frac{4rr_n}{(z-z_n)^2 + (r+r_n)^2}, \quad k_n'^2 \equiv 1 - k_n^2, \tag{8}$$

and $K(\cdot)$ and $E(\cdot)$ are complete elliptic integrals. The variable ξ_n is a regularization function given by

$$\xi_n = 1 - \exp\left[-\frac{(z-z_n)^2 + (r-r_n)^2}{\delta_n^2}\right]. \tag{9}$$

This regularization has been tested using a variety of validation calculations (Marshall & Grant 1997) and is found to perform well even in cases where $\delta_n/r_n = O(1)$.

The r- and z-components of the induced velocity in (7a) and (7c) are of the same form as used in the vortex method for non-swirling flow by Acton (1980). Strickland & Amos (1992) introduced an accelerated multipole expansion method for non-swirling axisymmetric flows, by which the number of calculations with N control points can be reduced from $O(N^2)$ to $O(N \ln N)$ per time step. No accelerated method has yet been developed for computation of swirling axisymmetric flows. The calculations can be considerably speeded up, however, with use of lookup tables for the elliptic integrals in (7a–c) and by storing a list of points near each fluid control point. More information on vortex methods in general can be found in review articles by Leonard (1985) and Meiburg (1995).

The velocity induced by the nth blob-like element is given by

$$\boldsymbol{u}_n(\boldsymbol{x},t) = \frac{P(\frac{3}{2}, |\boldsymbol{x}-\boldsymbol{x}_n|^2/R_n^2)\,\delta_n^3\,\pi^{1/2} C_n}{4|\boldsymbol{x}-\boldsymbol{x}_n|^3}\,\boldsymbol{G}_n \times (\boldsymbol{x}-\boldsymbol{x}_n), \tag{10}$$

where $P(a,z)$ is the incomplete gamma function, with limits $P = 0$ at $z = 0$ and $P =$

1 as $z \to \infty$, and C_n is the normalization constant given in (6). When $a = \frac{3}{2}$ and $z = x^2$, for some real variable x, a convenient expression for $P(\frac{3}{2}, x^2)$ is given in terms of the error function erf(x) as (Abramowitz & Stegun 1965)

$$P(\tfrac{3}{2}, x^2) = \mathrm{erf}(x) - \frac{2x\,\mathrm{e}^{-x^2}}{\pi^{1/2}}. \tag{11}$$

The element amplitudes are obtained via a collocation method, by fitting the vorticity representation (2) to the known vorticity values at the control points at every time step, using the approximate iteration procedure of Marshall & Grant (1996):

$$\boldsymbol{\omega}(\boldsymbol{x}_m, t) = \boldsymbol{G}_m^{(q+1)} \sum_{n \in Q(m)} W_{mn} + \sum_{n \in P(m)} W_{mn}\, \boldsymbol{G}_n^{(q)}, \tag{12}$$

where q is an iteration index, $Q(m)$ is a set of control points very close to control point m and $P(m)$ is the complement of $Q(m)$. The procedure (12) converges very quickly, and the number of iterations required for convergence seems to be independent of the number of control points. This iterative procedure can be used to simultaneously obtain the amplitudes of both the off-centre ring-like elements and the centre blob-like elements.

The self-induced velocity $\boldsymbol{w}_n$ of a ring-like element has the form

$$\boldsymbol{w}_n = \frac{G_\theta}{4\pi r_n}\left[\ln\left(\frac{8r_n}{\delta_n}\right) - C\right]\hat{z}, \tag{13}$$

where C is an $O(1)$ constant. Blob-like elements have no self-induced velocity. The importance of the element self-induced velocity, in comparison with the velocity induced by all of the other vorticity elements, depends on the resolution of the flow field. For instance, if the core of an isolated vortex ring is discretized by N ring-like elements, the ratio of the self-induced propagation velocity of an element to the propagation velocity of the ring as a whole is of order $1/N$. The effect of the element self-induced velocity was examined in numerical calculations by Strickland & Amos (1992) and Acton (1980), both of whom concluded that for a well-resolved vorticity field the element self-induced velocity is negligible.

For the computations presented in the present paper, the vorticity field is discretized using 3030 off-centre ring-like elements and 101 blot-like elements along the symmetry axis. Throughout §§2–6 of the paper, length variables are non-dimensionalized by the ambient core radius σ_0, velocity variables are non-dimensionalized by Γ/σ_0 and time is non-dimensionalized by σ_0^2/Γ. The control points in the (r, z)-plane were initially placed on a uniform grid in the region $0 \leqslant r \leqslant 1$ and $0 \leqslant z \leqslant 6$. The control point locations were then randomly displaced by an amount with maximum distance equal to 30% of the initial separation distance between the neighbouring points. The vorticity values at the control points and the control point locations are evolved in time using a second-order predictor-corrector method to solve (1) and (3).

The no-penetration condition on the cutting surface $z = 0$ is enforced by including a reflection of the computed vorticity field over this surface in the Biot–Savart integration. The other end of the computed vortex section is joined to a semi-infinite straight vortex filament of circulation Γ spanning the region $z > S$ (where $S = 6$ for the current computations), which induces a velocity $\boldsymbol{u}_s$ on any point (r, z) in the computational domain, given by Dhanak (1981) as

$$\boldsymbol{u}_s(r, z) = \frac{\Gamma r \boldsymbol{e}_\theta}{4\pi(r^2 + z^2)}\left\{1 - \frac{S - z}{[r^2 + (z - S)^2]^{1/2}}\right\}. \tag{14}$$

Case number	Axial flow parameter, A	Axial flow regime
C1	0.17	Subcritical
C2	0.51	Subcritical
C3	0.85	Supercritical

TABLE 1. Summary of computational cases considered. The axial flow regimes are determined using the critical value $A = 0.707$ predicted by the Lundgren–Ashurst plug-flow model.

The interval $5 < z < 6$ is a 'buffer region', in which upstream-propagating waves are damped out and the vorticity values are gradually brought to those on the initial plane. Control points are deleted when they cross the outer edge $z = 6$ of this buffer region, and new control points are created when any of 31 'boxes' spanning the radial direction at $z = 6$ are found to be empty. The exclusion distance, R_E, from the symmetry axis for ring-like elements is set to 50 % of the initial radial distance between neighbouring control points. Element radii, δ_n, are adjusted adaptively to be approximately twice the average distance from the given control point to the nearest four control points.

Issues of validation and verification of the computational method have been dealt with previously by Marshall & Grant (1997), who give comparisons with a number of exact solutions. For the computations reported in the present paper, we have verified that the time step and spatial resolution are sufficiently small by repeating runs with different values of the time step and different numbers of Lagrangian control points, and noting that the results are not noticeably different.

The evolution of the computed flow is governed by the axial flow parameter $A \equiv |2\pi\sigma_0 w_0/\Gamma|$, which represents the ratio of the mean axial velocity in the core to the characteristic swirling velocity. In this paper, computations are performed for three different values of this parameter, as listed in table 1. The mean axial velocity w_0 is obtained by numerical integration over the core cross-section, and the circulation Γ of the core is set by integrating the velocity in a circuit about the core with a radius of 1.5 in the initial configuration.

The Lundgren–Ashurst (1989) model, which assumes that the vortex has uniform axial velocity and vorticity within the core, predicts that the flow will be supercritical for $A > 0.707$ and subcritical for values of A less than this value. For a subcritical flow, both upstream- and downstream-propagating waves of small amplitude are possible, whereas for a supercritical flow only downstream-propagating waves of small amplitude are possible. While one cannot unambiguously apply this plug-flow model to the Gaussian vorticity profile considered in the current paper, a reasonable choice is to set the core radius and axial velocity of the vortex in the plug-flow model equal to the radial length scale σ_0 of the Gaussian vorticity distribution and the average axial velocity across a radial section of width σ_0 of the Gaussian vortex, respectively. This identification, together with the critical value $A = 0.707$ from the Lundgren–Ashurst model, is used to set the flow regimes for the computations in table 1.

3. Vortex response to cutting: expansion side

The Lundgren–Ashurst plug-flow model for axial motion on a vortex core with variable core area was used by Marshall (1994) to solve for the instantaneous cutting of a vortex which initially had non-zero axial velocity $w_0 < 0$ and uniform core radius.

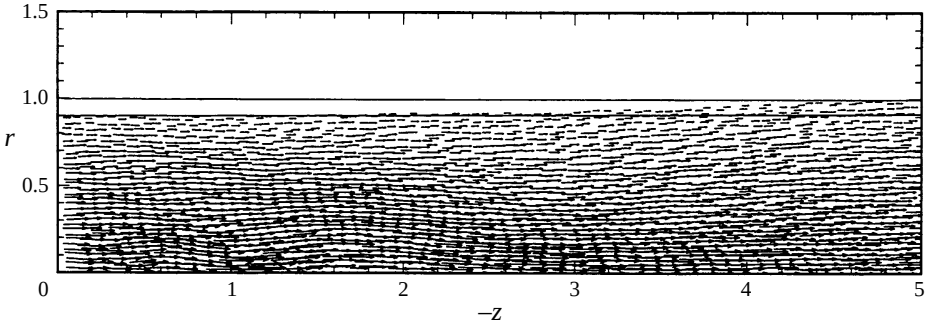

FIGURE 2. Vorticity vectors in the (r, z)-plane on the expansion side of the cutting surface, shown using an arrow attached to each Lagrangian control point, for the subcritical flow case C1. An expansion wave is observed to propagate on the vortex core, over which the core radius varies gradually. The core radius maintains a nearly constant value behind the expansion wave, indicated by the lower horizontal line in the figure. The plot is made at dimensionless time $t = 31.5$, at which point the front of the expansion wave has nearly reached the outer boundary of the computational domain.

The equations governing the core radius and axial velocity variation on a straight vortex core in the plug-flow model can be brought into correspondence with the one-dimensional gas dynamics equations, and thus admit a solution by the method of characteristics, such that

$$J^+ = w - 2c = \text{const} \quad \text{on} \quad \frac{\mathrm{d}z}{\mathrm{d}t} = w + c \quad (C^+ \text{ characteristics}), \tag{15a}$$

$$J^- = w + 2c = \text{const} \quad \text{on} \quad \frac{\mathrm{d}z}{\mathrm{d}t} = w - c \quad (C^- \text{ characteristics}). \tag{15b}$$

Here $w(z, t)$ is the local axial velocity within the vortex core, which is assumed to be uniform across the core cross-section, and c is the phase speed of long waves of infinitesimal amplitude on a vortex core with zero ambient flow, given in terms of the local core radius $\sigma(z, t)$ by

$$c = \frac{\Gamma}{\sqrt{8\,\pi\sigma}}, \tag{16}$$

when $\Gamma > 0$. On the expansion (downstream) side of the cutting surface (coinciding with $z < 0$ when $w_0 < 0$), an expansion wave forms at $t = 0$ and propagates downstream, such that the core radius changes linearly with axial distance between the rear, $z_R(t)$, and the front, $z_F(t)$, of the expansion wave, given by

$$z_F = (w_0 - c_0)\,t, \quad z_R = -c_B\,t. \tag{17}$$

Here c_B is the value of c near the cutting surface, behind the expansion wave, which is obtained using the conditions (15) as

$$c_B = c_0 - \tfrac{1}{2}w_0. \tag{18}$$

From (16) and (18), the ratio of core radius σ_B near the cutting surface to the initial core radius is obtained as

$$\sigma_B = [1 + \tfrac{1}{2}\sqrt{2\,A}]^{-1} \leqslant 1. \tag{19}$$

The predictions of the plug-flow model are compared with direct computations of the vortex response to instantaneous cutting, obtained using the vorticity collocation method described in §2, for different values of the swirl number. For instance, the vorticity field in the (r, z)-plane at a dimensionless time of $t = 31.5$ following cutting is shown in figure 2 for the subcritical flow case listed as C1 in table 1. In this plot, the

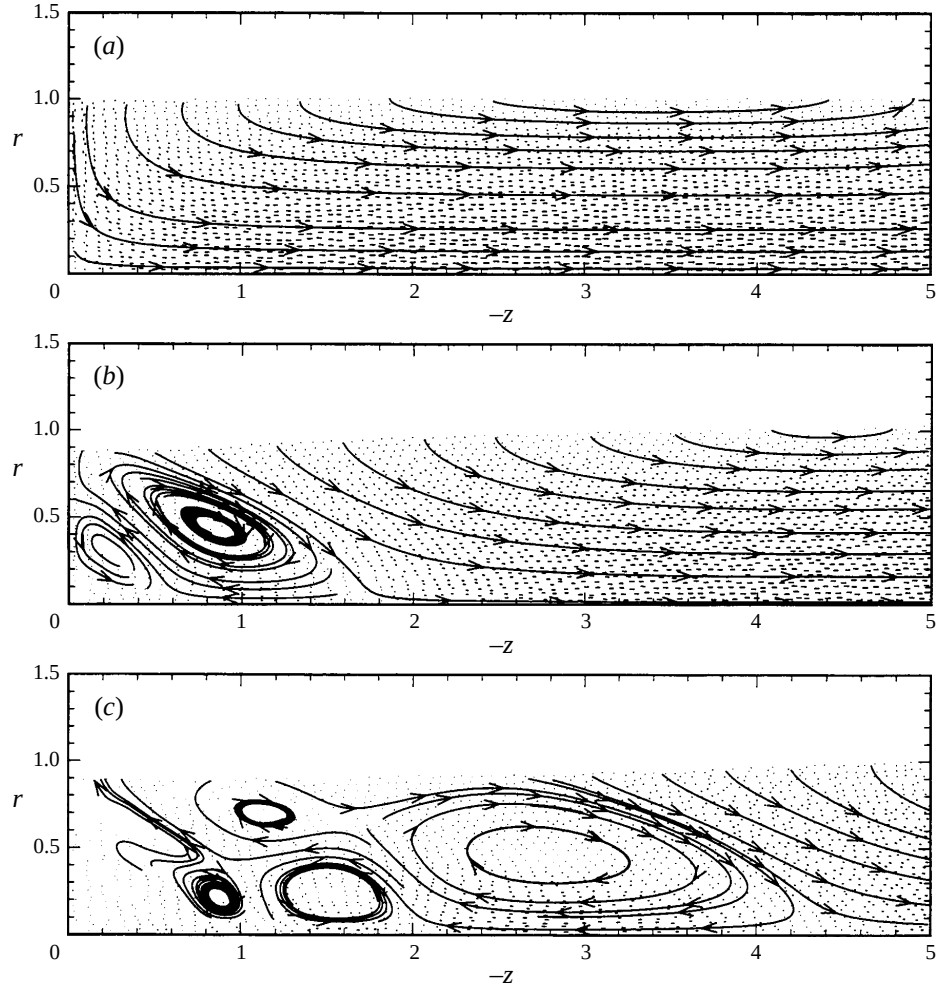

FIGURE 3. Streamlines in the (r, z)-plane on the expansion side of the cutting surface, for case C1. Short dashes are used to indicate the position of the vorticity control points. Plots are given at times (*a*) $t = 0.9$, (*b*) $t = 14.9$ and (*c*) $t = 30.9$. A series of vortex rings of alternating sign are observed to form within the expansion wave, which propagate downstream in time.

vorticity is plotted at each computational control point using a vector whose length is proportional to the vorticity magnitude. The vortex core radius is observed to vary gradually between a constant value of approximately 0.90 near the cutting surface $z = 0$ and the initial value of unity far away from the cutting surface. For this calculation, the prediction (19) of the plug-flow model gives $\sigma_B = 0.89$, which is the same as the computed value shown in figure 2.

The streamlines in the (r, z)-plane for this calculation are shown at three times in figure 3(*a–c*), where short dashes are used to denote the positions of the vorticity control points. In figure 3(*a*), the velocity near $z = 0$ is oriented radially inward due to the variation in axial velocity in the z-direction, resulting in a decrease in core radius near the cutting surface. In figure 3(*b*), a large vortex ring about the symmetry axis is observed within the columnar vortex core, where the clockwise circulation of the ring is oriented such that the fluid ahead of the ring is pulled radially inwards. A weaker secondary ring is observed behind the primary ring. The rings propagate along the

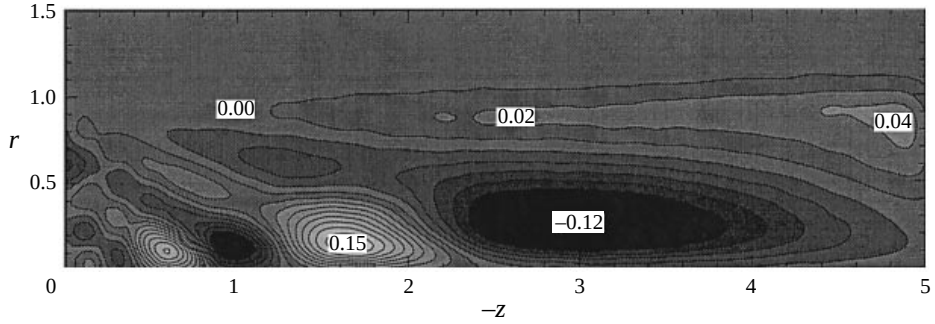

FIGURE 4. Contour plot of the azimuthal vorticity field, showing the trailing vortex system on the expansion side of the cutting surface, for case C1 at time $t = 30.9$.

vortex axis, such that at a later time, shown in figure 3(*c*), an extended train of vortex rings can be observed, which alternate in sign and become progressively weaker with distance behind the first ring. The effect of this series of vortex rings is to bring the velocity components in the (r, z)-plane gradually to zero in a region adjacent to the cutting surface, the size of which becomes progressively larger with time. The series of vortex rings thus plays essentially the same role as the rarefaction wave emitted by the impulsive withdrawal of a piston in a shock tube, in a reference frame travelling with the piston. The interval of gradual decrease of the core radius corresponds to the locations of the strongest few vortex rings, such that both behind and in front of these rings the core radius is nearly constant. The vorticity structure within the series of vortex rings is shown more clearly in the contour plot of the azimuthal vorticity field in figure 4, which corresponds to the same time as that for which the velocity vectors are shown in figure 3(*c*). Figure 4 both indicates the ring strengths and shows the alternating sign of azimuthal vorticity within the rings.

The swirl and radial components of the velocity field on the cutting surface for the subcritical flow case C1 are shown in figures 5(*a*) and 5(*b*), where plots are made at intervals of four dimensionless time units and the velocity profile at the initial time is indicated by a dashed curve. In figure 5(*a*), the peak value of the swirl velocity is found to initially increase in time, corresponding to a decrease in core radius, and to approach an asymptotic shape after which it does not change significantly. For all times, the swirl velocity converges onto a single curve for r greater than about unity, which indicates that the vortex circulation is well conserved during the computation. In figure 5(*b*), the radial velocity along the cutting surface is initially oriented inward, toward the symmetry axis. After some time, the radial velocity exhibits a change in sign with distance r on the cutting surface, which is due to the passage of vortex rings of alternating sign. Although the radial velocity profiles oscillate about the origin, the peak radial velocity is observed to become progressively smaller with time. Another indication of the presence of rings of alternating sign can be found in the plot of axial velocity versus distance along the symmetry axis, shown in figure 5(*c*). The axial velocity on the symmetry axis initially decreases monotonically to zero as the cutting surface is approached; however, after a short time the axial velocity is found to oscillate and exhibit alternate signs with distance along the symmetry axis. The axial flow reversals are caused by the presence of vortex rings of alternating sign propagating away from the cutting surface.

Other calculations for nearly critical and supercritical flows exhibit a similar propagating expansion wave, composed of a series of vortex rings of alternating sign,

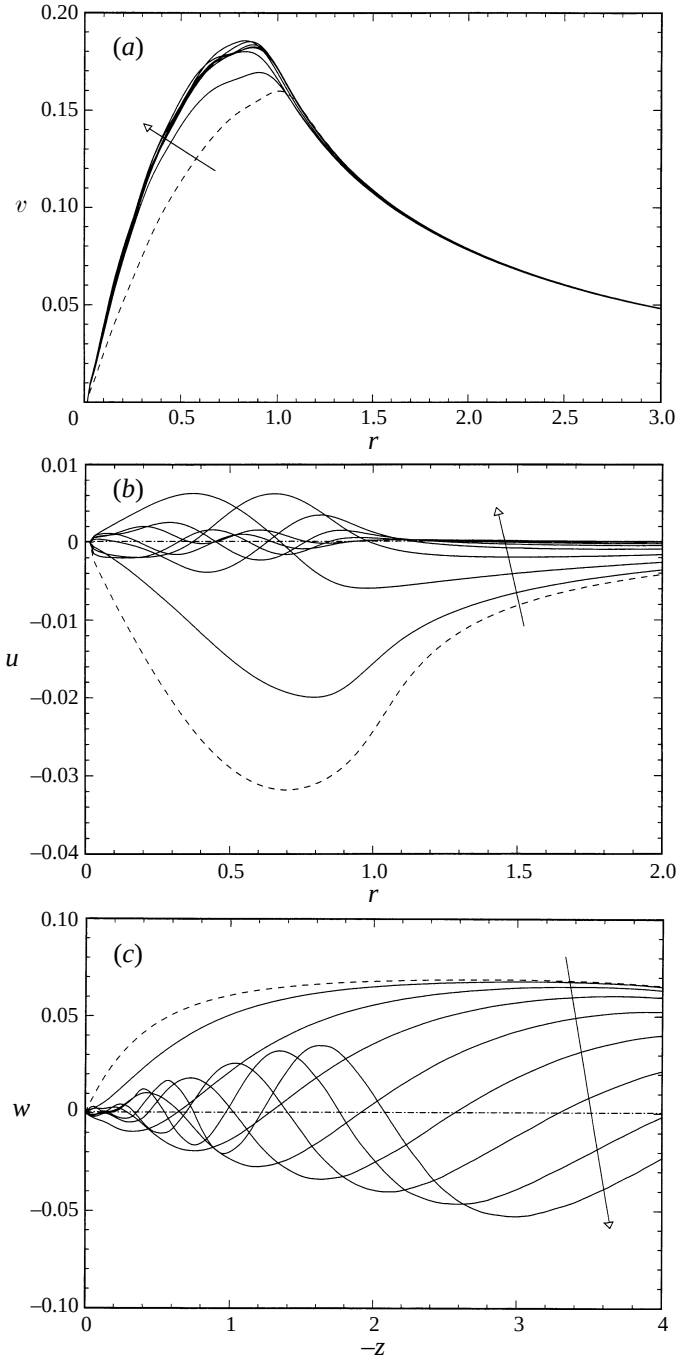

FIGURE 5. Time series of the variation of (*a*) the swirl and (*b*) the radial velocity components on the cutting surface ($z = 0$) and the variation of (*c*) the axial velocity on the symmetry axis ($r = 0$) for case C1 on the expansion side. Plots are made at intervals of 4 dimensionless time units, where the velocity profile at the initial time is indicated by a dashed curve. An arrow indicates the direction of time.

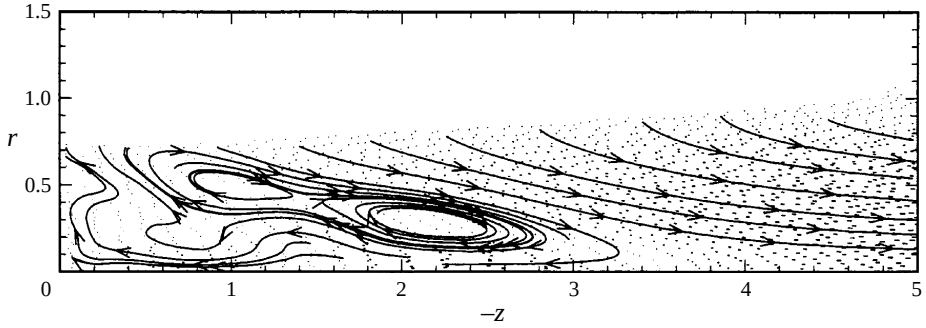

FIGURE 6. Streamlines in the (r, z)-plane on the expansion side of the cutting surface, for the nearly critical flow case C2, shown at time $t = 18.5$.

within the vortex core on the expansion side of the cutting surface. As predicted by (19), the core radius behind the expansion wave becomes progressively smaller as the value of A is increased. For instance, for the case C2 of a subcritical flow which is close to the critical point, a plot of the streamlines and the control point positions after the front of the expansion wave has nearly reached the far edge of the computed section of the vortex is shown in figure 6. For this case, the prediction (19) of the plug-flow model gives $\sigma_B = 0.735$, which nearly corresponds with the observed value in figure 6. As the value of A increases, the system of vortex rings associated with the expansion wave seems to primarily rotate in the clockwise direction, where the counter-clockwise rotating vortices observed in the subcritical flow shown in figure 4 appear to be suppressed. The vortex rings associated with the expansion wave also become more elongated in the streamwise direction as A is increased and the angle of the wedge made by the leading vortex ring becomes smaller.

The flow field on the expansion side for the supercritical flow case C3 appears qualitatively similar to that shown for nearly critical flow in figure 6. For this supercritical case, the core radius is observed to decrease near the cutting surface to a value of about 0.60, which corresponds fairly closely with the prediction $\sigma_B = 0.54$ from (19).

4. Vortex response to cutting: compression side

On the compression (upstream) side of the cut vortex, the plug-flow model predicts the formation of a vortex 'shock', or a discontinuity in core radius, which propagates upstream on the vortex (opposite to the direction of the ambient axial flow) at a velocity W. Expressions for the dimensionless shock propagation speed W and the core radius σ_B near the cutting surface (behind the shock) are obtained from jump conditions across the vortex shock (Marshall 1991, 1994) as

$$\sigma_B = \frac{1}{A}[(\sigma_B^2 - 1)\ln(\sigma_B)]^{1/2} \geqslant 1, \tag{20a}$$

$$W = \frac{1}{2\pi\sigma_B}\left[\frac{\ln(\sigma_B)}{\sigma_B^2 - 1}\right]^{1/2}. \tag{20b}$$

Equation (20a) admits solutions with $\sigma_B \geqslant 1$ for all values of the parameter A.

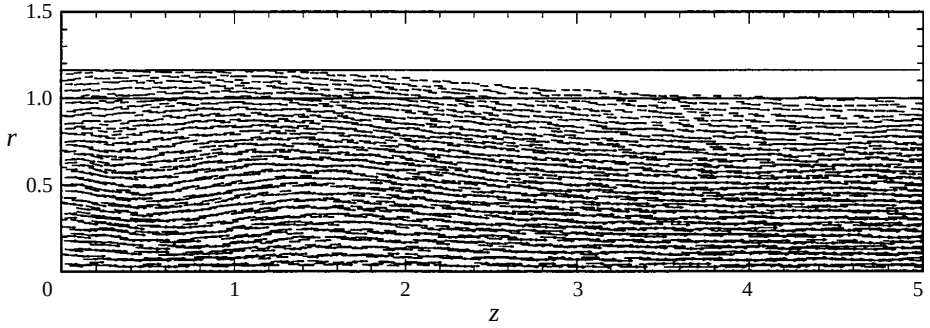

FIGURE 7. Vorticity vectors in the (r, z)-plane on the compression side of the cutting surface, for the subcritical flow case C1 at time $t = 30.9$. A compression wave is observed to propagate upstream on the vortex core, over which the core radius varies gradually. The core radius maintains a nearly constant value behind the compression wave, indicated by the upper horizontal line in the figure.

4.1. *Subcritical flow*

The result of a direct computation using the vorticity collocation method is shown in figure 7 for the vorticity components in the (r, z)-plane for the subcritical flow case C1. The core radius is observed to gradually decrease from a nearly constant value of about 1.16 near the cutting surface $z = 0$ to the ambient value of unit within a wave that propagates upstream on the vortex core. The prediction for σ_B from equation (20*a*) for this problem is about 1.14, which agrees closely with the observed value. Streamline plots in the (r, z)-plane for this flow are shown in figure 8(*a–c*) at three different times, where again the control point locations are indicated by short dashes. In figure 8(*a*), the velocity is oriented radially outward near the cutting surface due to the variation of the axial velocity in the z-direction, causing an increase in core radius. At later times (figure 8*b*), a counter-clockwise rotating vortex ring forms just upstream of the cutting surface, where the sense of circulation of the vortex is such as to cause an increase in core radius immediately upstream of the vortex location. The vortex ring propagates upstream and exhibits a trail of progressively weaker vortex rings of alternating sign behind it, as shown in figure 8(*c*). A contour plot of the azimuthal vorticity for the flow at a time corresponding to that used for figure 8(*c*) is given in figure 9, showing the alternating sign of azimuthal vorticity in the series of vortex rings.

Time series of the swirl and radial velocity profiles on the cutting surface ($z = 0$) are given in figures 10(*a*) and 10(*b*). In figure 10(*a*), the peak in swirl velocity is observed to decrease with time and to shift to the right, indicating an increase in vortex core radius. The swirl velocity profile converges to nearly the same curve at large r for all times, indicating again that vortex circulation is conserved during the computations. The radial velocity on the cutting surface (figure 10*b*) is initially oriented radially outward and decreases in time. After a short time, the radial velocity exhibits a sign change with radial distance, which is caused by the formation of upstream-propagating vortex rings at the cutting surface. The peak values of the radial velocity become progressively smaller with time. A time series of the variation of axial velocity with distance along the symmetry axis ($r = 0$) is plotted in figure 10(*c*). We again find that after sufficient time, the axial velocity changes sign, indicating a flow reversal associated with the passage of an upstream-propagating vortex ring. The magnitude of the axial velocity near the cutting surface also becomes progressively smaller with time.

For the case C2 of a subcritical flow that is close to the critical point, a very strong counter-clockwise rotating vortex ring is observed to form near the cutting surface

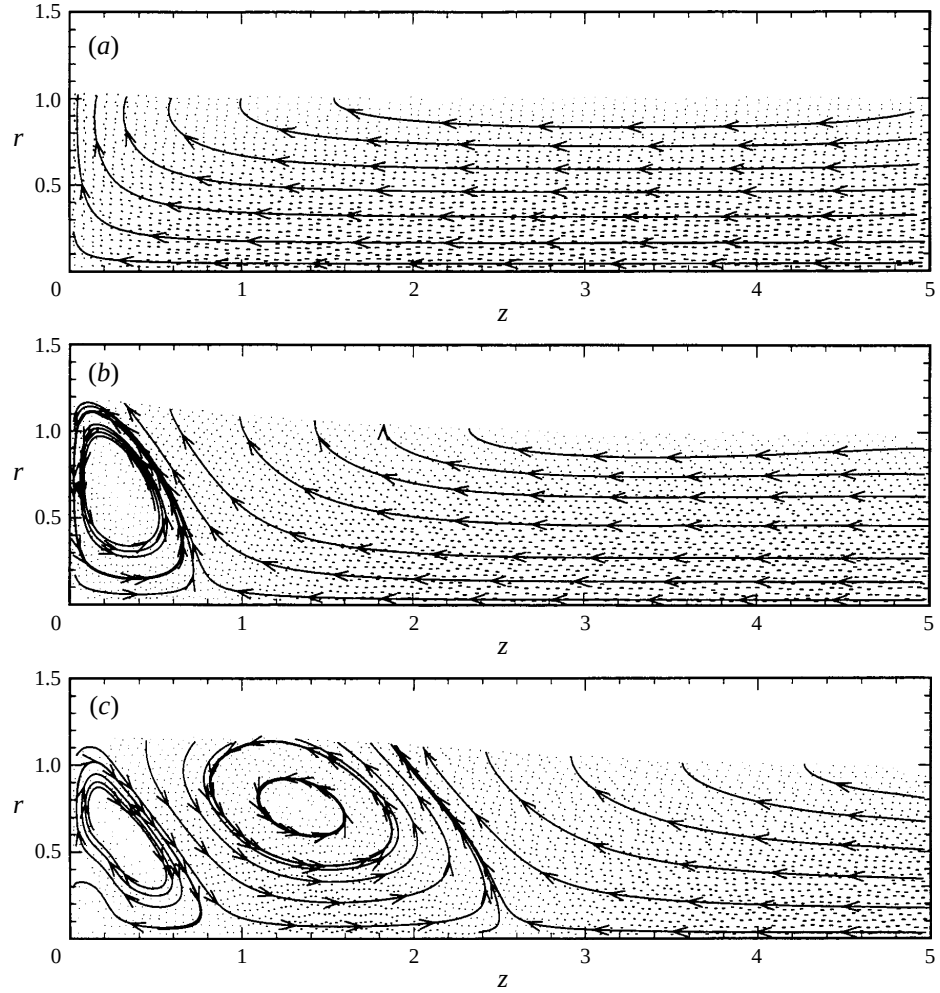

FIGURE 8. Streamlines in the (r, z)-plane on the compression side of the cutting surface, for case C1. Vorticity control points are indicated by short dashes. Plots are given at times (*a*) $t = 0.9$, (*b*) $t = 14.9$ and (*c*) $t = 30.9$. A series of vortex rings of alternating sign are observed to form within the compression wave, which propagate upstream in time.

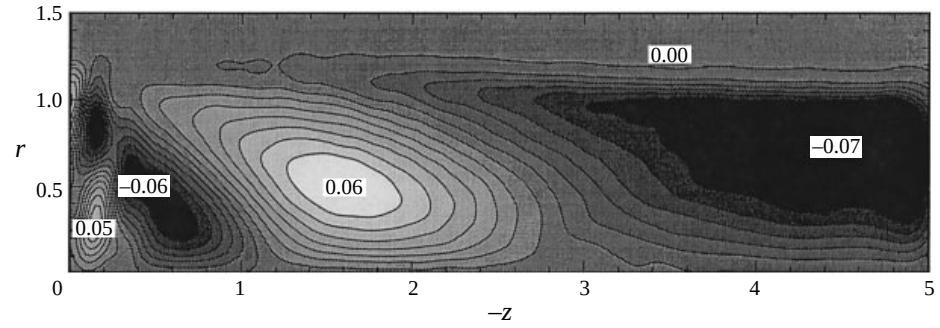

FIGURE 9. Contour plot of the azimuthal vorticity field on the compression side of the cutting surface, for case C1 at time $t = 30.9$.

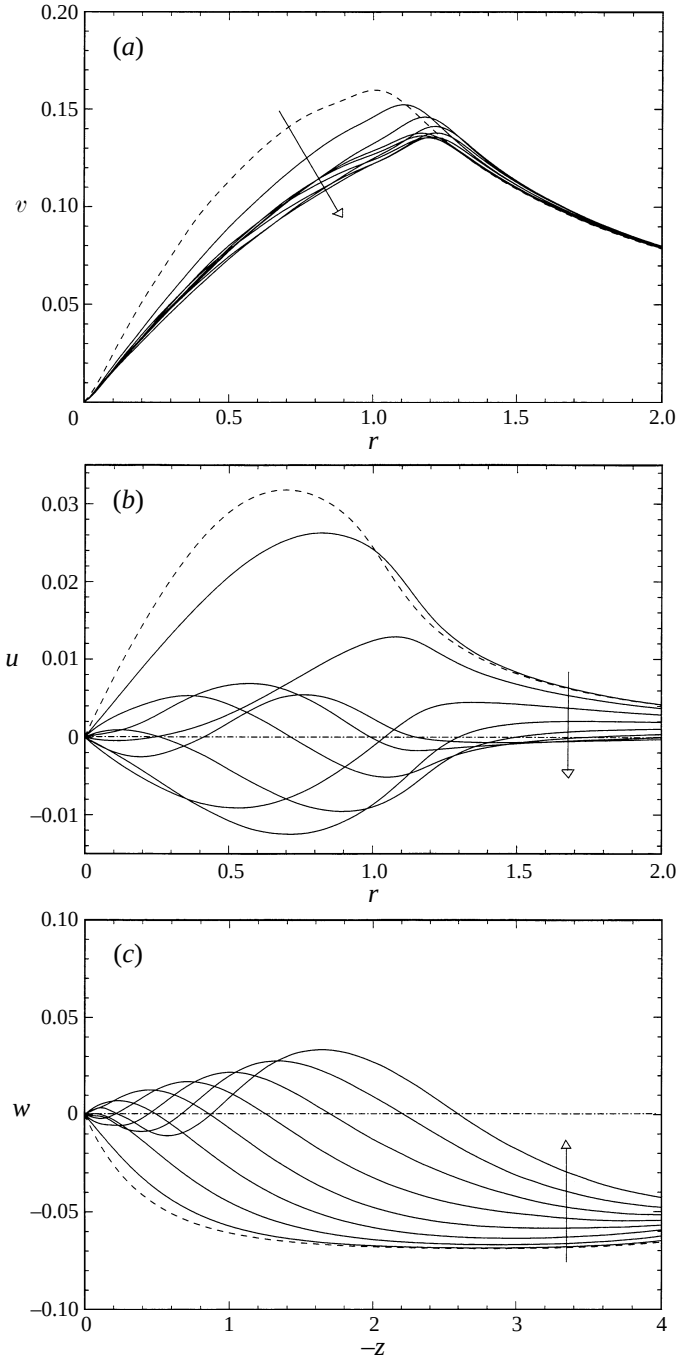

FIGURE 10. Time series of the variation of (*a*) the swirl and (*b*) the radial velocity components on the cutting surface ($z = 0$) and the variation of (*c*) the axial velocity on the symmetry axis ($r = 0$) for case C1 on the compression side. Plots are made at intervals of four dimensionless time units, where the velocity profile at the initial time is indicated by a dashed curve. An arrow indicates the direction of time.

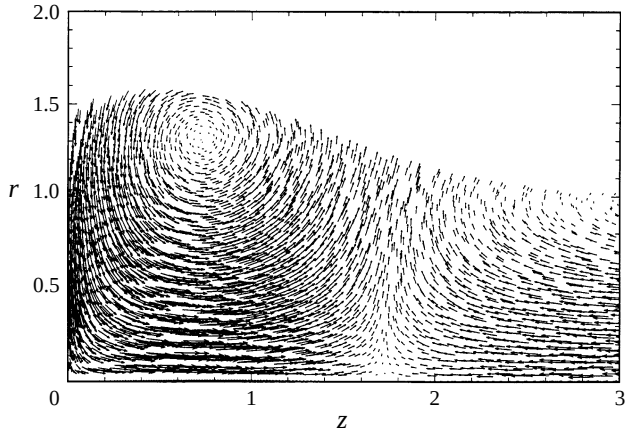

FIGURE 11. Close-up plot of the structure of a strong vortex ring just upstream of the cutting surface. The velocity vectors in the (r, z)-plane are shown, at time $t = 25.9$, on the compression side of the cutting surface for the nearly critical flow case C2. The vortex ring deflects the incoming axial flow in the radial direction, causing an increase in core radius just upstream of the vortex ring.

which propagates very slowly upstream. A close-up plot of the velocity vectors within this vortex ring is shown in figure 11, where the sense of the ring is such that the core radius is increased immediately upstream. It is noted that the axial velocity is upward (in the positive z-direction) immediately under the ring (opposite to the direction of the ambient flow) and that the velocity is oriented radially inward near the cutting surface in figure 11. The vortex core radius increases to roughly 1.5 near the cutting surface after the passage of the ring, whereas the theoretical prediction from (20*a*) for this case is $\sigma_B = 1.56$.

4.2. *Supercritical flow*

For supercritical flows, waves of alternating azimuthal vorticity are not able to propagate upstream and the vortex response on the compression side is hence quite different than that observed for subcritical flows. To illustrate these differences, streamline plots for the supercritical flow case C3 are shown in figure 12(*a–c*) at three different times, with locations of vorticity control points indicated by short dashes. The vortex flow is observed to impinge on the cutting surface in a manner qualitatively similar to that observed for a non-rotating fluid jet impacting on a wall, with no sign of upstream-propagating wave motion. At large time, the vorticity spreads radially outward on the cutting surface in the form of a thin propagating sheet of (principally) radial and azimuthal vorticity, which is slightly bulged near the leading edge.

While the streamlines within the vortex core are oriented principally in the streamwise direction (toward the cutting surface), backward-flowing streamlines are observed in the irrotational flow outside the vortex core. This backflow is suppressed in the computations of supercritical flow reported by Lee *et al.* (1995) due to use of a boundary condition of prescribed axial velocity on the right-hand side of the computational domain (which was set to zero outside of the vortex core). Since the equation for the Stokes streamfunction is elliptic, the boundary conditions can have a significant influence on the flow solution throughout the computed domain. In the current computations, the velocity is obtained from integration over the vorticity field in the Biot–Savart equation and it is not necessary to prescribe side boundary conditions on the velocity field. Rather, the only boundary conditions used in the

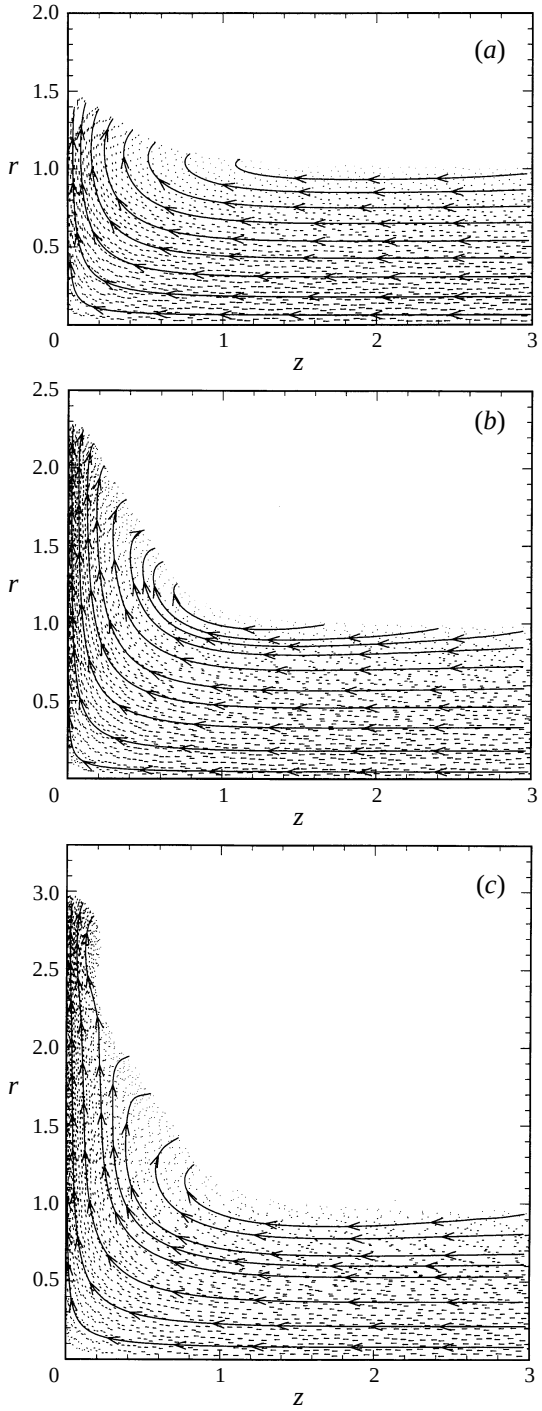

FIGURE 12. Streamlines in the (r, z)-plane on the compression side of the cutting surface for the supercritical flow case C3. Vorticity control points are indicated by short dashes. Plots are shown at times (*a*) $t = 3.9$, (*b*) $t = 11.9$ and (*c*) $t = 18.9$. The core radius continues to increase near the cutting surface, with no apparent upstream-propagating wave response on the vortex core.

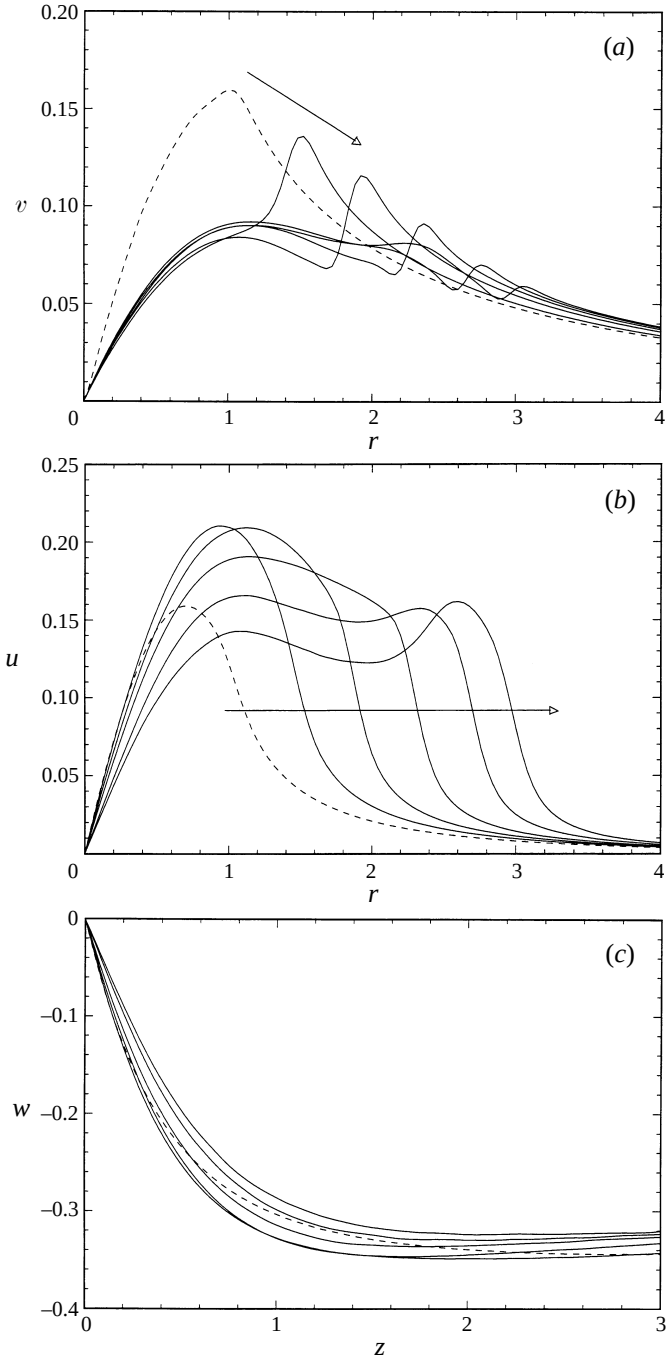

FIGURE 13. Time series of the variation of (*a*) the swirl and (*b*) the radial velocity components on the cutting surface ($z = 0$) and the variation of (*c*) the axial velocity on the symmetry axis ($r = 0$) for case C3 on the compression side. Plots are made at intervals of 4 dimensionless time units, where the velocity profile at the initial time is indicated by a dashed curve. An arrow indicates the direction of time.

present computations are the inlet condition on the vorticity field at the right-hand side of the domain and the condition of reflectional symmetry at the cutting surface (which is used to enforce the no-penetration boundary condition).

As noted by Lee *et al.* (1995), the flow near the point of impact of the vortex on the cutting surface seems to approach a steady state after sufficiently long time. For instance, the swirl and radial velocity components on the cutting surface ($z = 0$) are plotted as a function of radial distance for a series of times in figures 13(*a*) and 13(*b*), with the velocity at the initial time shown as a dashed line. The swirl velocity exhibits a peak near the outer part of the vortex core, where the magnitude of this peak becomes smaller as time increases. The swirl velocity clearly approaches an asymptotic curve near the end of the calculation for small values of r/σ_0, which extends increasingly outward with increasing time. The peak in radial velocity, shown in figure 13(*b*), initially increases in magnitude and then decreases again at long time. The radial velocity does not seem to be approaching an asymptotic shape for long time (as was observed for the swirl velocity), although it may do so if the run was extended for a longer time. The axial velocity is plotted versus distance along the symmetry axis in figure 13(*c*). The axial velocity profile does not seem to change much with time following impulsive cutting for supercritical vortices, as was also found by Lee *et al.* (1995).

5. Pressure variation and force on the cutting surface for subcritical flow

The pressure variation with radial distance on the cutting surface is computed using the radial component of the Euler equation:

$$\frac{\partial p}{\partial r} = -\rho\left(\frac{\partial u}{\partial t} + u\frac{\partial u}{\partial r} - \frac{v^2}{r}\right). \tag{21}$$

The pressure is evaluated at 200 points in the radial direction at $z = 0$, which are separated by a uniform spacing of $\Delta r = 0.05$ and extend out to a radius of 10. It is assumed that sufficiently far away from the vortex core, the pressure depends only on the vortex circulation and is unaffected by the core deformation near the cutting surface. We thus set the pressure equal to zero at $r = 10$ on both the expansion and compression sides, and integrate (21) for $r < 10$ using the standard trapezoidal scheme. The force on the cutting surface is obtained by subtracting the computed pressures on the expansion and compression sides of the cutting surface and then integrating over area. Throughout this section and the next, pressure is non-dimensionalized by $\rho\Gamma^2/\sigma_0^2$ and force is non-dimensionalized by $\rho\Gamma^2$.

Plots of pressure variation on the cutting surface for the subcritical flow case C1 are shown in figure 14(*a–c*) at three different times. Solid curves are used to indicate pressure on the compression side of the cutting surface and dashed curves are used for pressure on the expansion side. Following cutting of the vortex, the pressure increases on the compression side and decreases on the expansion side for r less than about 0.8, due to the change in swirl velocity corresponding to an increase in core radius on the compression side and a decrease on the expansion side. For r greater than about 0.8, the pressure on the expansion side becomes greater than that on the compression side, as shown in figure 14(*b*). This increase in pressure on the expansion side compared to that on the compression side for sufficiently large r is due to the unsteady $\partial u/\partial t$ term in (21), which (for short times) increases the radial pressure gradient on the compression side and decreases the pressure gradient on the expansion side (see figures 5*b* and 10*b*). The pressure on both sides of the cutting surface gradually approaches

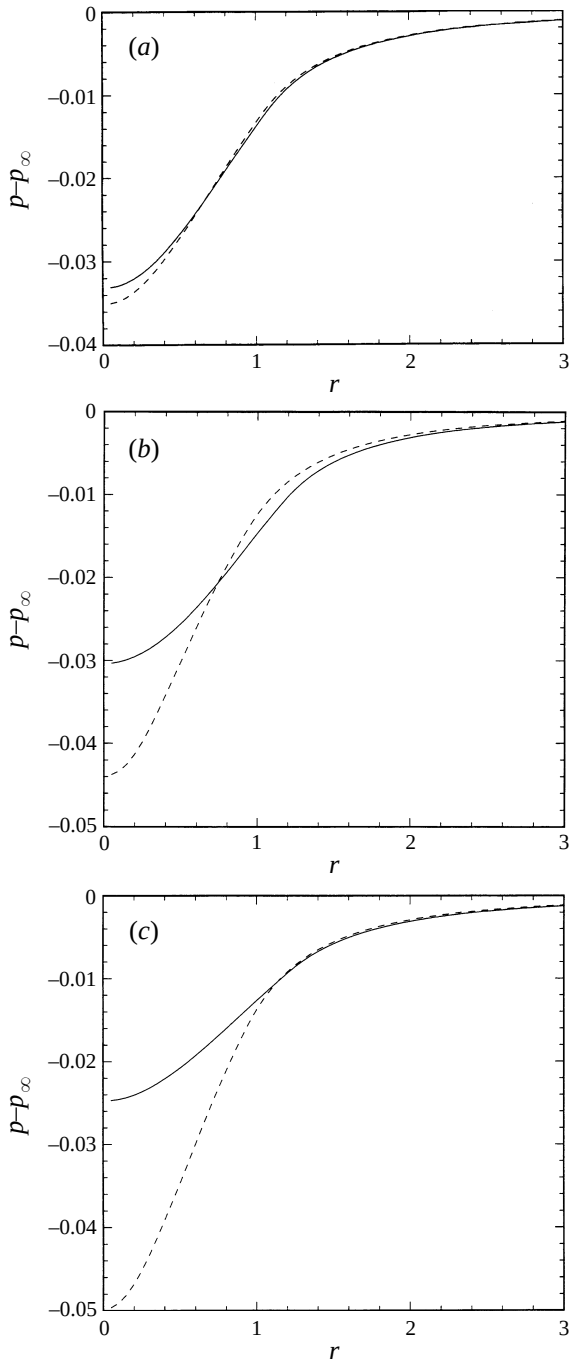

FIGURE 14. Pressure variation with radial distance on the cutting surface for case C1. The pressure on the compression side is drawn with a solid curve and that on the expansion side is drawn with a dashed curve. Plots are drawn at times (*a*) $t = 0.9$, (*b*) $t = 5.9$ and (*c*) $t = 30.9$. The pressure variation on both sides approaches an asymptotic profile, after which it does not change significantly with time.

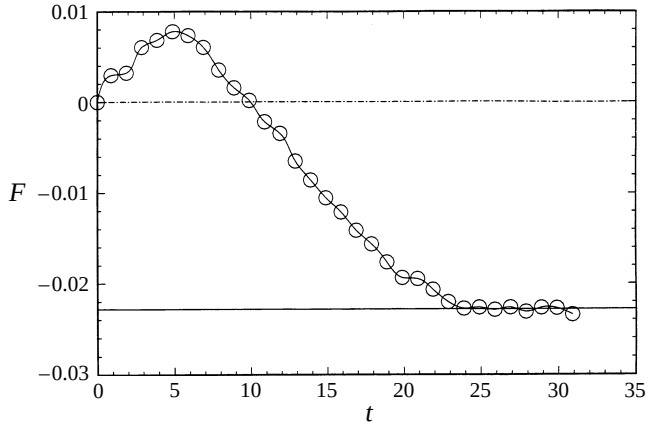

FIGURE 15. Variation of the net vortex-induced force on the cutting surface with time, for case C1. The force eventually attains an asymptotic value, indicated by a horizontal line, which is oriented in the same direction as the ambient axial flow.

an asymptotic profile (as shown in figure 14*c*), after which the pressure is nearly constant in time. This asymptotic profile corresponds to a condition in which the radial velocity nearly vanishes near the cutting surface (see figures 3*b*, 3*c* and 8*c*), such that the pressure is entirely determined by the swirling velocity profile. The pressure on the expansion side reaches this asymptotic profile more quickly than does that on the compression side, due to the faster propagation of the series of vortex rings on the expansion side, as shown by comparing figures 3 and 8.

The net force on the cutting surface is plotted in figure 15 for a computation of the subcritical flow case C1. The difference in pressure on the expansion side to that on the compression side is denoted by Δp, such that the net force on the cutting surface is given by the integral of Δp over the plane $z = 0$. We observe from figure 14(*b*) that for times immediately following vortex cutting, the pressure difference Δp is negative for small values of r and positive for larger r. While the peak positive value of Δp is smaller in magnitude than the peak negative value, the fact that the positive value occurs at larger radius gives it greater weight in calculation of the net force. We therefore find in figure 15 that for times immediately following vortex cutting, the net force on the cutting surface is directed upwards (opposite to the direction of the axial flow), due to the contribution of the region of positive Δp. For larger times, the magnitude of the positive Δp values gradually decreases and that of the negative Δp values increases, such that the net force on the cutting surface decreases. The pressure distributions on the cutting surface eventually approach asymptotic states on the two sides, in which the pressure on the cutting surface is controlled by the term proportional to v^2/r in (21) and Δp is everywhere negative. The net force on the cutting surface is therefore oriented downward (in the direction of the ambient axial flow) at larger times and eventually approaches an asymptotic value, which is indicated by the solid horizontal line in figure 15.

An estimate for the asymptotic value of the net force on the cutting surface after long time can be obtained by noting that the magnitude of the force due to a Rankine vortex of core radius σ, oriented normal to a plane surface, is simply

$$F = 2\pi \int_0^\infty p(r)\, r\, \mathrm{d}r = F_\infty + \frac{1}{4\pi}\ln(\sigma) - \frac{3}{16\pi}, \tag{22}$$

where F_∞ is a singular value that depends only on the vortex strength (and is independent of σ). The first and last terms on the right-hand side of (22) are the same for both sides of the cutting surface, so that the net force on the cutting surface (arising from the second term on the right-hand side of (22)) is simply

$$F = -\frac{1}{4\pi}\ln(\sigma_C/\sigma_E), \tag{23}$$

where σ_C and σ_E are the core radii on the compression and expansion sides, respectively. (An equation similar to (23) given in equation (38) of Marshall (1994) contained a typographical error, such that the predicted force was of the wrong sign.)

For the subcritical flow case C1, the observed values of σ_C and σ_E from figures 8(*c*) and 3(*c*) are about 1.16 and 0.90, respectively, so the net force on the cutting surface is predicted by (23) to be -0.020. The computed asymptotic value of the net force in figure 15 is about -0.023 for this case.

6. Pressure variation and force on the cutting surface for supercritical flow

Plots of pressure variation on the cutting surface for the supercritical flow case C3 are shown in figure 16(*a–c*) at three different times. The pressure is indicated by a solid curve on the compression side and by a dashed curve on the expansion side. On the expansion side of the cutting surface, the pressure decreases in time, due to the decrease in core radius, to an asymptotic profile in much the same way as was observed on the expansion side for subcritical flow. The asymptotic pressure profile on the expansion side is attained quite quickly, by a dimensionless time of about eight.

On the compression side of the cutting surface, the pressure initially increases for r less than about 0.8 and decreases for r greater than 0.8. The increase in pressure for small r is due both to the decrease in swirl velocity as the vorticity piles up near the cutting surface, as shown in figure 13(*a*), and to the increase in radial velocity with time, as shown in figure 13(*b*). The swirl velocity term in (21) leads to a positive slope of the pressure profile, whereas both radial velocity terms lead to a negative slope when u, $\partial u/\partial t$ and $\partial u/\partial r$ are all positive. The radial velocity terms seem to win this competition for r less than about 0.8 for short times, and the resulting pressure slope on the compression side is observed to be negative in this region in figures 16(*a*) and 16(*b*). At larger times, there is a gradual decrease in radial velocity near the cutting surface for small r (see figure 13*b*), which results in an increase in pressure gradient. The resulting pressure profile on the compression side seems to reach an almost asymptotic shape, given approximately by that shown in figure 16(*c*). In this profile, the pressure on the compression side is again larger than that on the expansion side for r less than about 0.8 and smaller than on the expansion side pressure for r between about 0.8 and 2.0. The pressure on both sides is nearly the same for r greater than about 2.0, except for some small waviness on the compression side due to the outward-propagating 'head' of the vorticity sheet which is spreading over the cutting surface.

We have found that for this supercritical flow case, the difference in pressure Δp on the expansion side to that on the compression side is negative for small radii and positive for larger radii. While the magnitude of the negative peak in Δp is generally considerably larger than that of the positive peak, the positive peak has a larger influence on the net force because it occurs at larger radii. The computed force F_r acting on a disk of radius r is plotted as a function of radius in figure 17 for the same three times as shown in figure 16(*a–c*). The regions of negative and positive Δp are found to

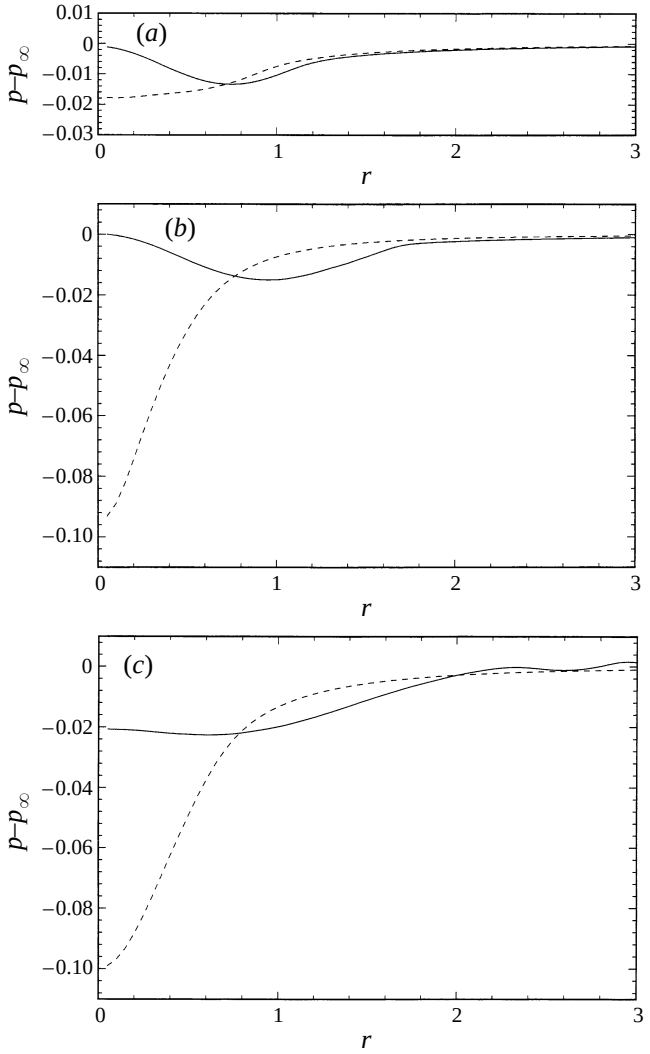

FIGURE 16. Pressure variation with radial distance on the cutting surface for case C3. The pressure on the compression side is drawn with a solid curve and that on the expansion side is drawn with a dashed curve. Plots are drawn at times (*a*) $t = 0.9$, (*b*) $t = 5.9$ and (*c*) $t = 18.9$.

have nearly an equal and opposite effect on the force on the cutting surface, such that F_r decreases to a peak negative value close to $r = 0.8$ and then increases again to nearly zero at $r = 2.0$. For r greater than 2.0, the pressures on both sides are nearly the same. The fact that the value of F_r at $r = 2.0$ is much less than its peak negative value for all cases considered leads to a state in which very small changes in pressure profile can produce large relative changes in the net force on the cutting surface. The computed force variation on the cutting surface, obtained by integrating pressure out to a radius of $r = 2.0$, is plotted as a function of time in figure 18. The net force values are found to be fairly small and rather noisy, since for the reasons stated previously, the net force is very sensitive to small pressure changes. For instance, the biggest force changes are observed to occur in figure 18 between dimensionless times of about 10 and 19, during which time the pressure profiles are close to their asymptotic values and are varying in time only very slightly.

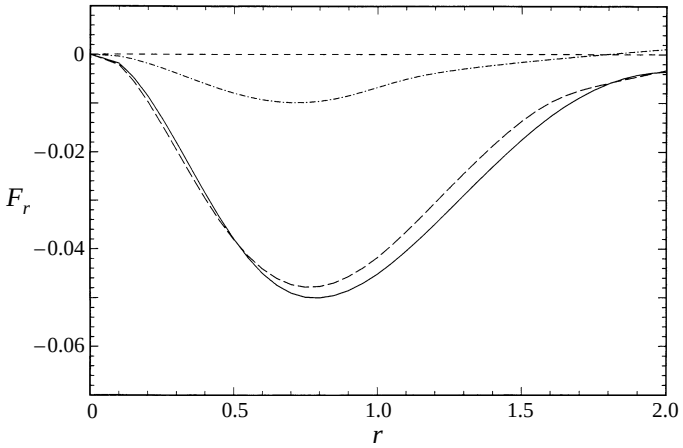

FIGURE 17. Variation of net force on a disk with radius r as a function of radius for case C3 at three different times: $t = 0.9$ (dashed-dotted curve), $t = 5.9$ (long dashed curve) and $t = 18.9$ (solid curve).

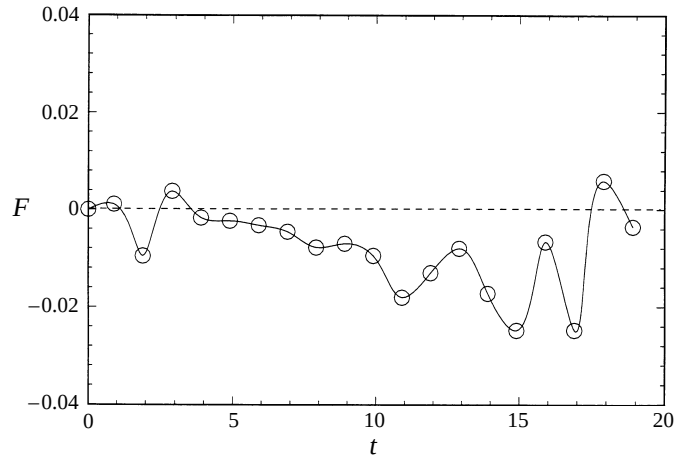

FIGURE 18. Variation of the net vortex-induced force on the cutting surface with time for case C3. The force is computed using a disk radius of $r = 2$.

7. Experimental determination of conditions for validity of the model

An experimental study was conducted to validate the instantaneous vortex cutting model, within a restricted flow regime, and to identify and assess the importance of flow features which are not included in this model. In these experiments, a thin blade in a horizontal position is translated through a vertical intake votex, with a downward ambient axial flow, and the response of both the primary vortex and the blade boundary layer are examined during the vortex cutting process. The experimental conditions allow examination of subcritical vortex flows only.

The primary vortex is generated in water in a cylindrical tank (30 cm diameter), about which is placed an outer rectangular tank (101 cm × 43 cm cross-section and 123 cm high) which is used to house the blade and support arms of the tow carriage. Water is circulated through the system via tangential inlet jets at the top of the inner cylindrical tank and an outlet orifice at the tank bottom. A steady intake vortex, with downward axial flow, is generated within about 20–30 minutes after starting the water

circulation along the centre axis of the inner cylindrical tank. The vortex is trapped at the top of the cylindrical tank by an inverted funnel, which both stabilizes the vortex and increases the core radius.

The blade has a symmetric Joukowski cross-section, with chord length $c = 152.4$ mm, maximum thickness $T = 6.4$ mm and span length of $b = 337$ mm. A gap with width of 24 mm exists in the inner cylindrical tank to leave room for passage of the blade. Flow visualization was used to ensure that the blade boundary layer is not significantly affected by passage through the gap. A part of the blade near the leading edge was hollowed out to serve as a dye reservoir, and five dye ports (0.34 mm diameter) placed in a row along the blade span provide a means to dye the blade boundary layer. The blade is towed across the vortex by a frame driven by a variable-speed computer-controlled screw drive, which provides smooth blade translation over a wide range of speeds. During each run, the blade is accelerated to a prescribed speed U over a specified distance, which is set such that the blade traverses the entire inner cylinder at a constant speed.

The laser-induced fluorescence (LIF) technique is used for flow visualization, with dyes that fluoresce at two different colours. The primary vortex is visualized using red fluorescent dye (Sulfurhodamine 640) and the blade boundary layer is visualized with yellow fluorescent dye (Rhodamine chloride 590). The dyes are excited by a light sheet from a continuous 300 mW argon-ion laser source, which is oriented to illuminate a vertical slide of the vortex. Photographs are taken using both a 35 mm still camera and a standard video camera, with frame rates of approximately 4 and 30 frames per second, respectively. The green laser light is filtered out so that only the emitted light of the dyes are recorded on film. A sketch showing the relative orientation of the primary vortex, the blade, the laser sheet and the camera is given in figure 19.

The yellow dye is gravity fed into the blade boundary layer from an external reservoir, and its flow rate can be finely controlled by adjusting the gravity head and a needle valve placed in the feed time. Preliminary tests were performed without the vortex present to ensure that the injection of yellow dye does not disturb the blade boundary layer.

Red dye is injected into the primary vortex at the top of the inner cylindrical tank, and carried downward by the ambient axial flow within the vortex core. For times shortly after dye injection, the entire core of the vortex is filled with red dye. However, as time passes, the dye within the inner part of the core becomes depleted, leaving red dye only in the outer layers of the core where the axial velocity is much lower than at the core centre.

The circulation of the primary vortex is measured using neutrally buoyant immiscible dye globules (bromobenzene and paraffin oil mixed in proportion along with a fat soluble dye), which are released through a hypodermic needle close to the plane of blade motion and well outside the vortex core. The axial velocity distribution in the vortex core is determined from video recordings of dye globules (1–2 mm in diameter) injected into the core at the top of the internal cylindrical tank at different radii, which are then carried downward into the vortex core by the ambient axial flow. The data points for the axial velocity distribution are fit to a Gaussian curve, of the form

$$w(r) = w_{max} \exp(-r^2/\sigma_0^2). \tag{24}$$

For the vortex settings used in the experiments reported in this section (see table 2), the axial velocity data and best fit Gaussian curve are shown in figure 20. The Gaussian fit yields a core radius of $\sigma_0 = 10 \pm 2$ mm and a maximum axial velocity of $w_{max} =$

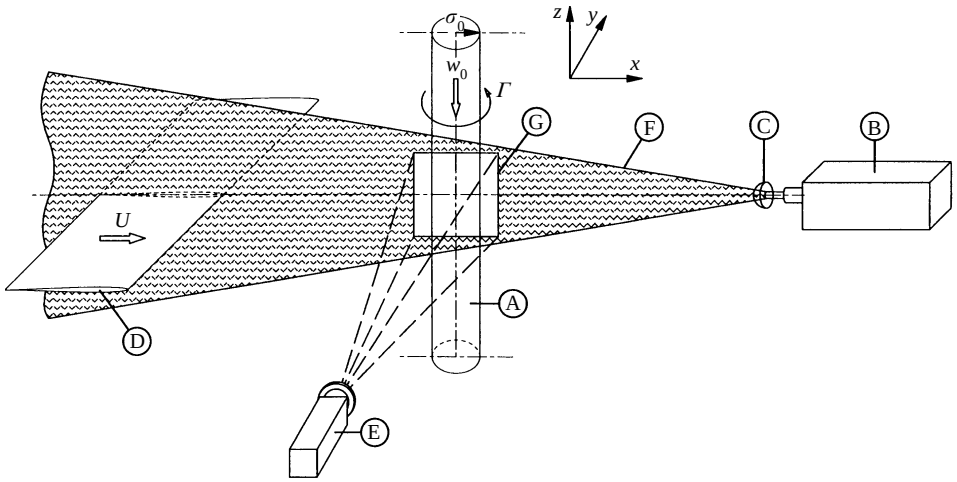

FIGURE 19. Sketch of the experimental apparatus, showing orientation of the blade (D), the primary vortex (A), the laser light sheet (F) with the photographed section (G), and the camera (E). Also shown are the continuous laser (B) and the cylindrical lens (C).

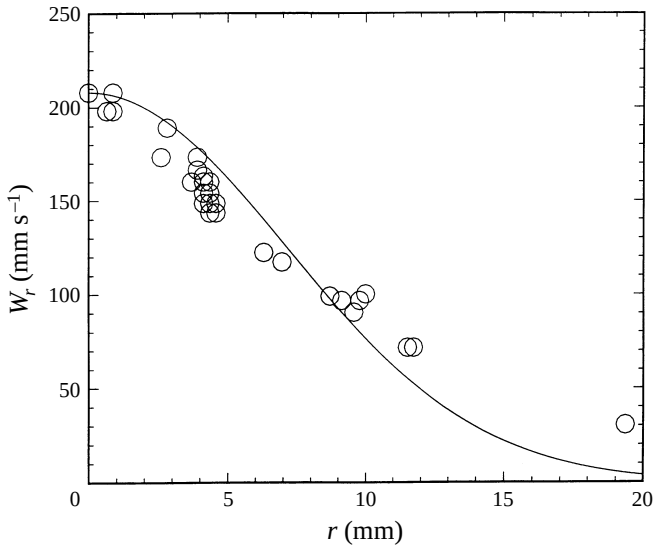

FIGURE 20. Data for axial velocity within the primary vortex core as a function of radial distance from the centre of the inner cylindrical tank, together with the best-fit Gaussian curve.

FIGURE 21. Photograph showing a thin blade interacting with a columnar vortex (red), as illuminated by a laser sheet, with downward axial flow w_0, for the case E1 in the 'wrapping' regime. The vortex centreline is about 19 mm ahead of the blade leading edge. The circulation is in a counter-clockwise direction from a perspective looking down on the blade from above. A scale of 1 cm is indicated by two vertical lines on the lower right-hand side of the figure, and the blade has been digitally inserted into the photograph. A slice of the legs of a secondary hairpin vortex structure, formed of (yellow) vorticity which has been ejected from the blade boundary layer and wrapped around the primary vortex, is indicated by the label [A].

FIGURE 23. Photograph showing the vortex response on the compression side for case E2 at a time when the vortex centreline is located at about half the blade chord. A scale of 1 cm is indicated by two horizontal lines in the lower left-hand side of the figure. The upward-propagating compression wave is indicated by the label [A]. Helical waves following the compression wave are indicated by [B]. [C] indicates the front of the entrained boundary layer fluid (yellow), and [D] indicates the top surface of the blade.

Figure 21. For caption see page 67.

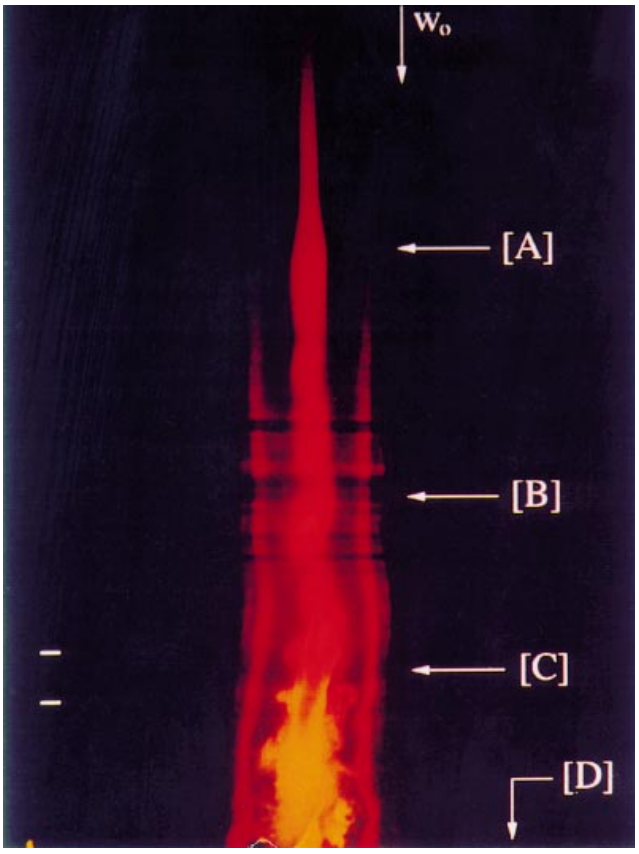

Figure 23. For caption see page 67.

(*a*)

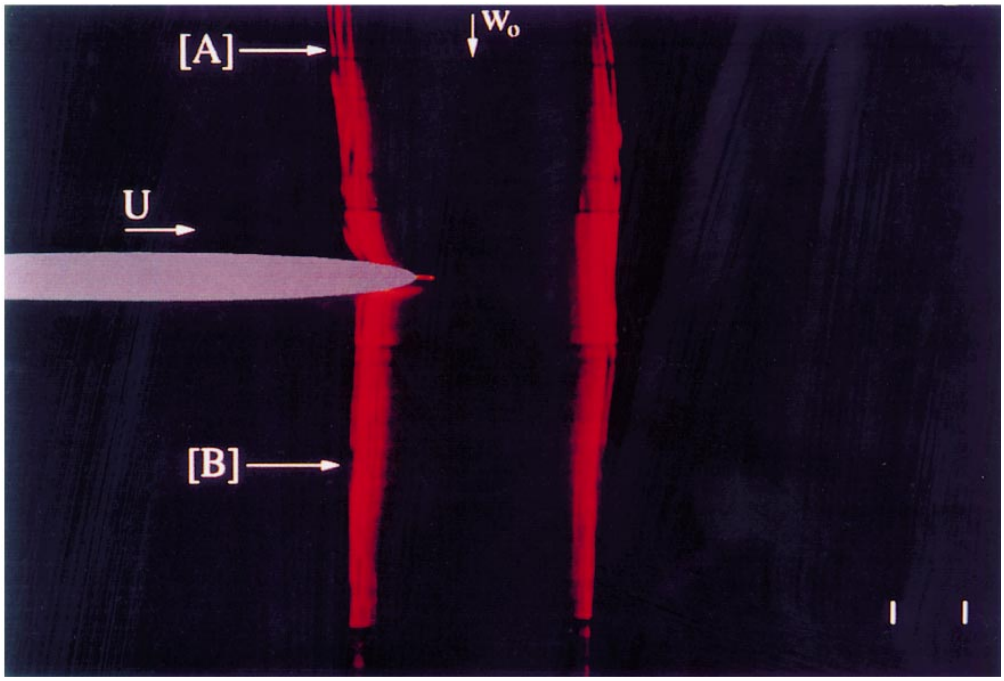

(*b*)

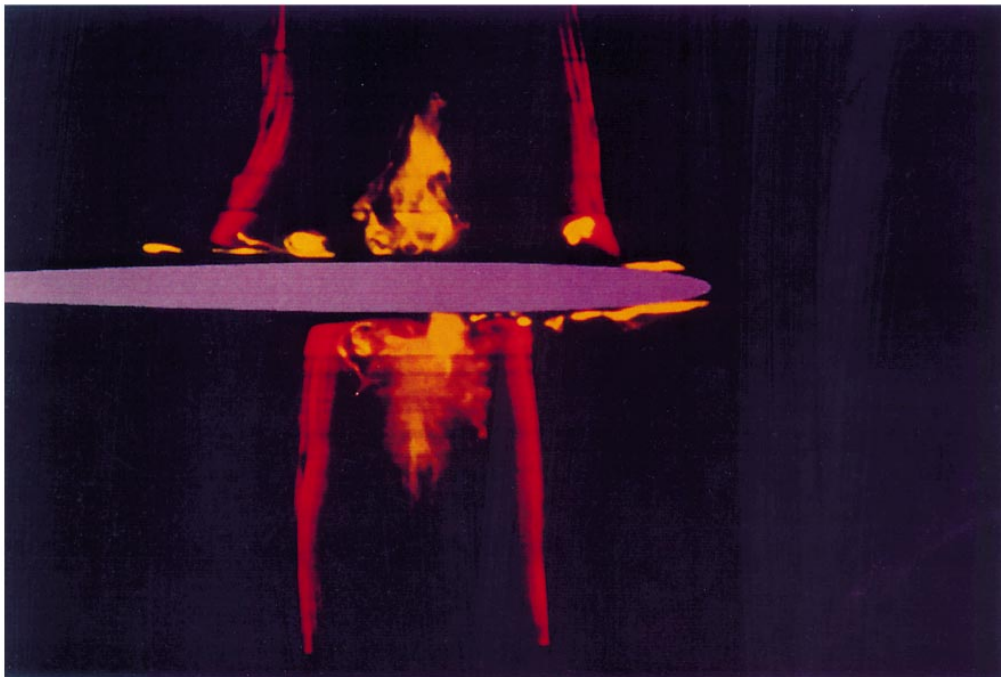

FIGURE 22. For caption see page 70.

Case number	$2\pi\sigma_0 U/\Gamma$	$2\pi\sigma_0 w_0/\Gamma$	Blade–vortex interaction regime
E1	0.055	0.2	Wrapping regime
E2	0.31	0.2	Cutting regime

TABLE 2. Summary of experimental cases reported.

208 ± 8 mm s^{-1}. The average axial velocity over the core radius σ_0 is $\bar{w} = 131 \pm 5$ mm s^{-1}, and the circulation is obtained as $\Gamma = 40\,901 \pm 2285$ mm^2 s^{-1}. These parameters indicate that the vortex is in a subcritical state, with axial flow parameter $A = 0.20 \pm 0.05$ and vortex Reynolds number $Re_V \equiv \Gamma/\nu = 4.1 \times 10^4$.

With the vortex parameters cited above kept constant, the blade was translated across the vortex core at speeds U ranging from 20 to 300 mm s^{-1}, thus enabling substantial variation in the parameter $2\pi\sigma_0 U/\Gamma$. The blade Reynolds number $Re_B \equiv Uc/\nu$ is varied in these experiments from about 3000 to 46 000. A 'wrapping' regime is observed for values of U such that $2\pi\sigma_0 U/\Gamma$ is less than about 0.08, in which the vortex–blade interaction is characterized by ejection of boundary layer vorticity from the blade prior to impact with the vortex and subsequent wrapping of this secondary vorticity about the primary vortex core. The secondary vorticity appears to take the form of one or more hairpin structures. For instance, a visualization showing a slice of the legs of a secondary hairpin vortex (yellow dye) after it has wrapped roughly one loop about the primary vortex (red dye) is shown in figure 21 for a case with $2\pi\sigma_0 U/\Gamma = 0.055$. The blade has been inserted digitally in the photograph. The smaller the value of $2\pi\sigma_0 U/\Gamma$, the earlier the secondary vorticity separation occurs and the more chance the secondary vortex has to loop about the primary vortex. The wrapping process appears to culminate in the impingement of the hairpin nose on the primary vortex core, leading to a rapid disruption of the primary vortex.

Of more interest in the present work are cases where the value of $2\pi\sigma_0 U/\Gamma$ is sufficiently high that this vorticity wrapping process does not occur. We have identified such a regime, which we call the 'cutting' regime, for values of U in which $2\pi\sigma_0 U/\Gamma$ is greater than about 0.24. In this regime, there is no separation of the blade boundary layer prior to impingement of the blade onto the vortex core. As we shall show, boundary layer separation does occur at a later stage in the interaction process, both due to the impingement of the vortex axial flow on the blade tip during the initial cutting of the vortex and due to entrainment of boundary layer fluid into the severed vortex core following cutting. However, in the cutting regime the separated boundary layer fluid stays confined within the primary vortex core and does not exhibit the extensive wrapping external to the core which is typical of the wrapping regime. A gradual transition between these two regimes occurs in the range of intermediate values of the parameter $2\pi\sigma_0 U/\Gamma$.

The vortex response in the cutting regime was examined in detail for a case with

FIGURE 22. Photographs showing a blade penetrating into and cutting through a columnar vortex in the 'cutting' regime for case E2. In (*a*), the blade has just begun penetrating into the vortex core, and the blade boundary layer remains attached. The compression and expansion sides of the vortex are indicated by the labels [A] and [B], respectively. In (*b*), the blade has cut through the vortex core. The increase in the primary vortex core radius on the compression side and the decrease on the expansion side, as well as the entrainment of boundary layer fluid, are clearly visible in this figure. The vortex centreline is located at a distance of about 10 mm ahead of the blade leading edge in (*a*) and 39 mm behind the blade leading edge in (*b*).

$2\pi\sigma_0 U/\Gamma = 0.31$. Photographs visualizing the region close to the intersection of the blade and the primary vortex are shown at two times during the cutting process in figures 22(*a*) and 22(*b*). The primary vortex is visualized by two red bands along the outer edges of the vortex core, where the radius of these red bands far away from the blade is about 17–20 mm, or roughly twice the core radius σ_0 as determined from figure 20. In figure 22(*a*), the blade leading edge has just penetrated the primary vortex core. At this stage, the yellow dye remains in the blade boundary layer and the primary vortex bends about the blade surface in a manner similar to that predicted by Marshall & Grant (1996).

Figure 22(*b*) shows the vorticity response after the blade has cut through the primary vortex core. A considerable difference in core radius is observed between the compression and expansion sides of the primary vortex, with both a 'local' variation in radius very close to the blade surface and a 'far-field' variation at a distance of about a core radius from the blade surface. Using the far-field values for the core radius, the estimated ratio of core radii on the two sides of the blade is obtained from figure 22(*b*) as $\sigma_{comp}/\sigma_{exp} \approx 1.4$. Equations (19) and (20*a*), using the plug-flow model, predict this ratio to be 1.33 under the conditions used in the experiments, showing rough agreement. The abrupt local expansion of the core radius on the compression side, which is not observed in the inviscid flow calculations, is believed to be due to radial expansion of the core caused by entrainment of the blade boundary layer fluid, as visualized by the yellow dye.

The boundary layer fluid (yellow dye) is observed to become entrained and propagate away from the blade on both the compression and expansion sides, travelling somewhat faster on the expansion side as might be expected. (Note that the thin black strip in figure 22(*b*) very near the blade surface is the shadow of the blade and does not indicate lack of yellow dye). While the primary vortex is initially in a laminar state, the entrained boundary layer vorticity exhibits a multitude of complex small-scale vortical structures which spiral within the primary vortex core. The entrained vorticity thus forms a front of turbulence which propagates away from the blade on both sides of the primary vortex core. However, the time scale of the entrained vorticity is much greater than that of the inviscid response of the vortex core to cutting, so that the inviscid model may still be a reasonable approximation for the vortex response immediately after cutting.

To demonstrate this point, a photograph is presented in figure 23 which shows the vortex response to cutting on the compression side over a longer axial distance than in the previous figures. The plane of blade passage is close to the bottom of the photograph, and the photograph was taken when the vortex centreline is located at about half the blade chord. The red dye was injected into the primary vortex at a later time than in figure 22, so that in addition to the outer region of the core visualized in figure 22, the red dye is also apparent within the inner core. The compression wave which is generated as the vortex is cut by the blade is observable in this picture as a red bulge, which travels upward in time at a speed of 320 ± 5 mm s^{-1}. This value compares reasonably well with the predicted 'shock' speed of 365 mm s^{-1}, obtained from solution of equation (20*b*) using the experimentally measured vortex parameters. By contrast, the propagation speed of the (yellow) entrained boundary layer fluid for this case is observed to be 95 ± 5 mm s^{-1}, which is about a third of the compression wave speed. A more extensive comparison of experimental vortex compression wave speeds and predictions for vortex 'shocks' is given by Krishnamoorthy & Marshall (1994). Related discussions of boundary layer entrainment into vortex structures have been given by Hagan & Kurosaka (1993) and Cohn & Koochesfahani (1993).

Another limitation on the axisymmetric cutting model used in the current paper is the formation of helical waves on the primary vortex behind the compression wave. The helical waves initially have wavelengths of about 10 mm (roughly equal to the core radius) and amplitudes that are much smaller than the core radius. The helical waves are visible in figure 23 from about two-thirds of the distance between the blade and the compression wave all the way to the blade surface, although the wave amplitudes in this photograph are small. In a fixed position along the vortex axis, both the wavelength and the amplitude of the helical waves are observed to grow slowly with time, such that at a much later time than shown in figure 23 the helical waves are quite pronounced.

8. Conclusions

A computational study of the vortex response to impulsive cutting is reported for inviscid axisymmetic flows. On the expansion side of the vortex, a series of vortex rings are observed to propagate away from the cutting surface (in the direction of the ambient axial flow). Behind these vortex rings, the axial and radial components of the velocity vector nearly vanish and the core radius is reduced. The vortex response on the compression side depends on the magnitude of the ambient mean axial velocity w_0 in comparison to the phase speed c of azimuthal vorticity waves on the core. When $w_0 < c$, so that the flow is subcritical, a series of upstream-propagating vortex rings of alternating sign is observed, behind which the radial and axial components of velocity are reduced to nearly zero and the core radius is increased. When $w_0 > c$, so that the flow is supercritical, upstream-propagating waves are not possible, and the axial flow impinges on the cutting surface much like a non-swirling jet might impinge on a flat plate.

A variety of results for the computed flows have been compared with the predictions of an approximate analytical solution of this problem (Marshall 1994) using a simple plug-flow model for subcritical flows. These include the variation in vortex core radius on the expansion and compression sides of the vortex, the propagation speed of the upstream compression wave and the normal force exerted on the cutting surface. In all cases, the comparison with the plug-flow model is quite close, even though the structure of the vorticity fields within the computed expansion and compression waves differ considerably with that assumed in formulating this model.

An experimental flow-visualization study of the impact of a thin blade on a vortex core is also reported, in order to validate the results of the impulsive vortex cutting model. The experiments indicate that the assumption of impulsive vortex cutting is reasonably valid only when the relative speed of the blade and the vortex is sufficiently high that the blade boundary layer does not separate prior to impingement of the blade on the vortex core ($2\pi\sigma_0 U/\Gamma$ larger than about 0.24). Besides this restriction, the inviscid model does not include the entrainment of boundary layer vorticity into the primary vortex core. Similarly, the axisymmetric model does not include the formation of helical waves which are observed on the primary vortex during the later stages of the vortex–blade interaction. Both of these effects exhibit time scales which are much longer than that associated with the inviscid vortex response, and thus restrict the time interval following vortex cutting over which the inviscid axisymmetric model is valid. Aside from these various restrictions, most of the main qualitative flow features of the computational solutions using the instantaneous cutting model are also observed in the experiments, including an increase in core radius and the formation of an upstream-propagating compression wave on the compression side of the vortex and a decrease

in core radius on the expansion side. Quantitative comparison between the experimentally observed values for propagation speed of the compression wave and the variation in vortex core radius with the theoretically predicted values also yields reasonable agreement.

The authors are grateful to A. T. Conlisk for making them aware of the paper by Lee *et al*. (1995). Funding for this research was provided by the US Army Research Office under grant number DAAH04-96-1-0081 to The University of Iowa. Dr Thomas L. Doligalski is the program manager. Computer time was provided by a grant from the San Diego Supercomputing Center.

REFERENCES

Abramowitz, M. & Stegun, I. A. 1965 *Handbook of Mathematical Functions*. Dover.

Acton, E. 1980 A modelling of large eddies in an axisymmetic jet. *J. Fluid Mech.* **98**, 1–31.

Affes, H. & Conlisk, A. T. 1993 Model for rotor tip vortex-airframe interaction. Part 1: Theory. *AIAA J.* **31**, 2263–2273.

Affes, H., Conlisk, A. T., Kim, J. M. & Komerath, N. M. 1993 Model for rotor tip vortex-airframe interaction. Part 2: Comparison with experiment. *AIAA J.* **31**, 2274–2282.

Affes, H., Xiao, Z. & Conlisk, A. T. 1994 The boundary layer flow due to a vortex approaching a cylinder. *J. Fluid Mech.* **275**, 33–57.

Ahmadi, A. R. 1986 An experimental investigation of blade-vortex interaction at normal incidence. *AIAA J. Aircraft* **23**, 47–55.

Amiet, R. K., Simonich, J. C. & Schlinker, R. H. 1990 Rotor noise due to atmospheric turbulence ingestion. Part 2. Aeroacoustic results. *AIAA J. Aircraft* **27**, 15–22.

Bagai, A. & Leishman, J. G. 1992 Experimental study of rotor wake/body interactions in hover. *J. Am. Helicopter Soc.* **37**, 48–57.

Cary, C. M. 1987 An experimental investigation of the chopping of helicopter main rotor tip vortices by the tail rotor. *NASA CR*-177457.

Cohn, R. K. & Koochesfahani, M. M. 1993 Effect of boundary conditions on axial flow in a concentrated vortex core. *Phys. Fluids* A **5**, 280–282.

Dhanak, M. R. 1981 Interaction between a vortex filament and an approaching rigid sphere. *J. Fluid Mech.* **110**, 129–147.

Doligalski, T. L., Smith, C. R. & Walker, J. D. A. 1994 Vortex interactions with walls. *Ann. Rev. Fluid Mech.* **26**, 573–616.

Hagen, J. P. & Kurosaka, M. 1993 Corewise cross-flow transport in hairpin vortices – the 'tornado effect'. *Phys. Fluids* A **5**, 3167–3174.

Howe, M. S. 1988 Contributions to the theory of sound production by vortex-airfoil interaction, with application to vortices with finite axial velocity defect. *Proc. R. Soc. Lond.* A **420**, 157–182.

Howe, M. S. 1989 On unsteady surface forces, and sound produced by the normal chopping of a rectilinear vortex. *J. Fluid Mech.* **206**, 131–153.

Johnston, R. T. & Sullivan, J. P. 1992 Unsteady wing surface pressures in the wake of a propellor. *AIAA Paper* 92-0277.

Kim, J. M. & Komerath, N. M. 1995 Summary of the interaction of a rotor wake with a circular cylinder. *AIAA J.* **33**, 470–478.

Krishnamoorthy, S. & Marshall, J. S. 1994 An experimental investigation of 'vortex shocks'. *Phys. Fluids* **6**, 3737–3741.

Lee, J., Xiao, Z., Burggraf, O. R., Conlisk, A. T. & Komerath, N. M. 1995 An inviscid analysis of vortex-surface collisions. *AIAA Paper* 95-2237.

Leonard, A. 1985 Computing three-dimensional incompressible flows with vortex elements. *Ann. Rev. Fluid Mech.* **17**, 523–559.

Leverton, J. W., Pollard, J. S. & Wills, C. R. 1977 Main rotor wake/tail rotor interaction. *Vertica* **1**, 213–221.

Liou, S. G., Komerath, N. M. & McMahon, H. M. 1990 Measurement of the interaction between a rotor tip vortex and a cylinder. *AIAA J.* **28**, 975–981.

Lundgren, T. S. & Ashurst, W. T. 1989 Area-varying waves on curved vortex tubes with application to vortex breakdown. *J. Fluid Mech.* **200**, 283–307.

Marshall, J. S. 1991 A general theory of curved vortices with circular cross-section and variable core area. *J. Fluid Mech.* **229**, 311–338.

Marshall, J. S. 1994 Vortex cutting by a blade. Part 1: General theory and a simple solution. *AIAA J.* **32**, 1145–1150.

Marshall, J. S. & Grant, J. R. 1996 Penetration of a blade into a vortex core: vorticity response and unsteady blade forces. *J. Fluid Mech.* **103**, 83–109.

Marshall, J. S. & Grant, J. R. 1997 A Lagrangian vorticity collocation method for viscous, axisymmetric flows with and without swirl. *J. Comput. Phys.* (in press).

Marshall, J. S. & Yalamanchili, R. 1994 Vortex cutting by a blade. Part 2: Computations of vortex response. *AIAA J.* **32**, 1428–1436.

Meiburg, E. 1995 Three-dimensional vortex dynamics simulations. In *Fluid Vortices* (ed. S. I. Green), pp. 651–686. Kluwer.

Saffman, P. G. 1970 The velocity of viscous vortex rings. *Stud. Appl. Maths* **49**, 371–380.

Sheridan, P. F. & Smith, R. P. 1980 Interactional aerodynamics – A new challenge to helicopter technology. *J. Am. Helicopter Soc.* **25**, 3–21.

Simonich, J. C., Amiet, R. K., Schlinker, R. H. & Greitzer, E. M. 1990 Rotor noise due to atmospheric turbulence ingestion. Part 1. Fluid mechanics. *AIAA J. Aircraft* **27**, 7–14.

Stickland, J. H. & Amos, D. E. 1992 Fast solver for systems of axisymmetric ring vortices. *AIAA J.* **30**, 737–746.